

UNSTABLE BAR AND SPIRAL MODES OF DISK GALAXIES

MIR ABBAS JALALI¹ AND C. HUNTER²

Department of Mathematics, Florida State University, Tallahassee, FL 32306-4510

Submitted to The Astrophysical Journal

ABSTRACT

We study bisymmetric modes of angular wavenumber 2 for flat stellar disks in potentials with smooth cores. Stars either all circulate in the same direction or a small fraction may counter-rotate. The bisymmetric modes are unstable unless there is a sufficiently large external halo or bulge. We find two modes for each disk: a more central fundamental mode and a more extensive and more spiral (trailing) secondary mode. The fundamental mode is particularly sensitive to the orbital population in the central part of the disk. Depending on that population, it varies from a small compact bar to a trailing spiral that is almost as wound as the secondary mode. All modes rotate too rapidly for there to be an inner Lindblad resonance. They transfer angular momentum from the central to the outer regions of the disk. Most of them release gravitational energy and convert it to kinetic energy, which also flows outwards through the disk.

Subject headings: stellar dynamics, galaxies: kinematics and dynamics, galaxies: spiral, galaxies: structure

1. INTRODUCTION

The publication by Lin & Shu (1964) of a density wave theory of spiral structure generated wide interest, and has led to a broad literature. One strand of that literature consists of stellar dynamic studies of the instabilities of flat stellar systems. Important ingredients of the analysis of Lin & Shu are the approximations of tight-winding, or near-axisymmetry, of the waves, and of the near-circularity of the stellar orbits of the unperturbed disk. A key result obtained using these approximations is that of Toomre (1964) who showed that the stability of stellar disks to axisymmetric waves requires that the parameter $Q = \kappa\sigma_R/3.36G\Sigma_D > 1$. Here κ is the epicyclic frequency, σ_R is the radial velocity dispersion, Σ_D is the disk density, and G is the gravitational constant. This result has proved to be remarkably robust and widely applicable, despite the simplifying approximations used in its derivation. Yet it was soon recognized that Toomre's criterion does not provide a complete stability criterion for stellar disks when N -body experiments (Miller, Prendergast & Quirk 1970, Hohl 1971, Ostriker & Peebles 1973) revealed that disks with Q safely greater than 1 are prone to large-scale barlike instabilities.

Kalnajs (1971,1977) developed the matrix method for using linear perturbation theory to study the stability of stellar systems. His method is quite general and does not impose any restrictions on the forms of either the instability, or the unperturbed stellar orbits. The matrix method is sufficiently complex that it has not been widely used, though that is gradually changing. The first comprehensive study using it was that of Zang (1976) who analyzed the instabilities of scale-free singular isothermal disks. Some of the results of his PhD thesis are given in papers by his supervisor (Toomre 1977, 1981). Zang's methods were re-used and extended by Evans & Read (1998a,b) who analyzed singular scale-free disks with other power-law rotation laws. Scale-free disks have the

property that the orbits at any energy are simply scaled versions of those at any other energy. Though this is indeed a simplification, even applications of the matrix method to scale-free disks are by no means simple.

We study stellar disks with smooth and non-singular cores. One of the main purposes of our work is to understand the influence that orbital populations have on the responses of the disks to density perturbations, by studying the responses of a variety of disks. That variety allow us to study the effects of the mass and extent of the disk, the orbital population, and a central bulge. In §2.1 we use the matrix method to derive the eigenvalue problem whose outcome is the pattern speed, growth rate and mode shape of an unstable galactic disk. We show in §2.2 that a boundary integral, which has been unjustifiably ignored in some earlier work, may occur with unidirectional disks. In §2.3 we extend the linear perturbation theory to second order. Those results are needed for studying how modes transfer angular momentum and potential and kinetic energy. In §2.4 we discuss Polyachenko's (2004) simplified theory of spiral and bar-like modes. In later sections we compare our findings with its predictions.

We introduce the three axisymmetric potentials which we use for our models in §3. They are those of Kuzmin's disk, the isochrone disk, and the cored logarithmic potential. We use known distribution functions (DFs) for stellar disks with the first two potentials. However, none are currently available for cored exponential disks embedded in the cored logarithmic potential, and so we construct some DFs for them in §3.5. Lastly in §3.6 we discuss a way to model the effects of hot central bulges by modifying DFs by cutting out a part of their orbital population.

We describe our computational procedures in §4. In §5 we give the results of our computations of modes of angular wavenumber $m = 2$ obtained using the matrix method. Some of our models are new, while others are the same as those studied in prior work. The prior work, some of which was done using carefully applied N -body simulations, includes that of Kalnajs (1978), Earn

¹ E-mail: mjalali@math.fsu.edu

² E-mail: hunter@math.fsu.edu

& Sellwood (1995) and Pichon & Cannon (1997) for the isochrone potential, and that of Athanassoula & Sellwood (1986), Sellwood & Athanassoula (1986), Hunter (1992), and Pichon & Cannon (1997) for Kuzmin's potential. Vauterin & Dejonghe (1996) studied modes of a cored exponential disk, like that we use in §3.4, in a potential with a nearly flat rotation curve, which they obtained by combining two Kuzmin potentials. Sellwood (1989) studied modes of the uncored and mildly singular exponential disk in the same cored logarithmic potential as we use for our models in §5.3.

In §6 we discuss and interpret our computational results. We summarize our results in §7.

2. PERTURBATION THEORY

This section presents the dynamical theory on which our work is based. §2.1 carries out an Eulerian linear perturbation analysis of the collisionless Boltzmann equation in action-angle variables. We derive a matrix eigenvalue problem for finding modes, following Kalnajs (1971, 1977). We apply this analysis to unidirectional disks in which all stars circulate in the same direction in §2.2, and show that the matrix formulation must then include additional boundary integral terms. We extend the perturbation theory to second order in §2.3 to the extent necessary for discussing the transfer of angular momentum, and kinetic and potential energy. In §2.4 we discuss orbits and their responses, and relate the analysis of §2.1 to Polyachenko's (2004) theory.

2.1. Linear Perturbation Theory

We study the stability of a collisionless stellar disk composed of a distribution of stars moving in orbits in a circularly symmetric potential $V_0(R)$. The unperturbed system is described by a DF $f_0(E, L)$ (Binney & Tremaine 1987) where

$$E = \frac{1}{2}(v_R^2 + v_\phi^2) + V_0(R), \quad L = Rv_\phi, \quad (1)$$

are the energy and angular momentum which remain constant along an orbit. The density corresponding to the unperturbed DF is

$$\Sigma_D = \int f_0 d\mathbf{v}, \quad (2)$$

where $d\mathbf{v}$ denote an element of the two-dimensional velocity space. This density is the one that produces the potential $V_0(R)$ only in the fully self-consistent case; in our work it often provides only a part of that potential. The development of the DF for the perturbed state is described by the collisionless Boltzmann equation

$$\partial f / \partial t + [f, \mathcal{H}] = 0, \quad (3)$$

where $[,]$ denotes a Poisson bracket and \mathcal{H} is the Hamiltonian

$$\mathcal{H} = \frac{1}{2}(v_R^2 + v_\phi^2) + V(R, \phi, t). \quad (4)$$

We expand the DF as $f = f_0 + f_1 + f_2 + \dots$ and the Hamiltonian as $\mathcal{H} = \mathcal{H}_0 + V_1 + V_2 + \dots$, where $V = V_0 + V_1 + V_2 + \dots$ is the corresponding expansion of the potential. Collecting terms of first and second orders then gives the equations

$$\frac{\partial f_1}{\partial t} + [f_1, \mathcal{H}_0] = -[f_0, V_1], \quad (5)$$

$$\frac{\partial f_2}{\partial t} + [f_2, \mathcal{H}_0] = -[f_0, V_2] - [f_1, V_1]. \quad (6)$$

It is necessary that the perturbed densities due to the changes from the unperturbed DF are precisely those needed to produce the corresponding components of the perturbed density, so that

$$V_j(\mathbf{x}, t) = -G \int \frac{\Sigma_j(\mathbf{x}', t) d\mathbf{x}'}{|\mathbf{x} - \mathbf{x}'|}, \quad j \geq 0, \quad (7)$$

$$\Sigma_j(\mathbf{x}, t) = \int f_j(\mathbf{x}, \mathbf{v}, t) d\mathbf{v}, \quad j > 0. \quad (8)$$

Here $d\mathbf{x}$ and $d\mathbf{v}$ denote elements of the two-dimensional position and velocity spaces. Equation (7) is true when $j = 0$ because we shall use Σ_0 to denote the self-consistent density for the potential V_0 . Equation (2) replaces the $j = 0$ case of equation (8).

It is convenient to work with the action variables of the unperturbed motion, defined by

$$J_R = \frac{1}{2\pi} \oint v_R dR, \quad J_\phi = L. \quad (9)$$

The first equation here defines J_R as a function of E and L . The actions provide an alternative pair of integrals of motion, in terms of which we can express the unperturbed DF $f_0(J_R, J_\phi)$ and Hamiltonian $\mathcal{H}_0(J_R, J_\phi)$. The advantage of using action variables is that their conjugate angle variables (θ_R, θ_ϕ) increase uniformly with time

$$\frac{d\theta_R}{dt} = \frac{\partial \mathcal{H}_0}{\partial J_R} = \Omega_R(J_R, J_\phi), \quad \frac{d\theta_\phi}{dt} = \frac{\partial \mathcal{H}_0}{\partial J_\phi} = \Omega_\phi(J_R, J_\phi). \quad (10)$$

Perturbations must be periodic in the angles, and this allows us to use Fourier series in these angles for them (Kalnajs 1971). It is convenient to write these Fourier series in the complex form

$$f_1 = e^{i(m\theta_\phi - \omega t)} \sum_{l=-\infty}^{\infty} \tilde{f}_l(J_R, J_\phi) e^{il\theta_R}, \quad (11)$$

$$V_1 = e^{i(m\theta_\phi - \omega t)} \sum_{l=-\infty}^{\infty} \tilde{V}_l(J_R, J_\phi) e^{il\theta_R}, \quad (12)$$

with the understanding that it is their real parts which give the physical solution. Following Landau (1946), we suppose that the frequency ω is complex with real and imaginary parts

$$\omega = m\Omega_p + is, \quad (13)$$

with Ω_p representing an angular pattern speed and s a growth rate. We suppose initially that $s > 0$ so that we have a growing disturbance which was infinitesimally small infinitely long ago. The possibility of stationary oscillations and real values of ω has to be considered via analytical continuation to $s = 0$ from $s > 0$.

The solutions (11) and (12) are those for a perturbation of a single angular wavenumber m . Perturbations of all angular wavenumbers are possible and could be considered (Kalnajs 1971, Lynden-Bell & Kalnajs 1972) but we forgo that generality. Different wavenumbers do not interact at the first order when as here, the unperturbed state is axisymmetric. In fact we shall be concerned almost entirely with the case of $m = 2$.

Substituting expansions (11) and (12) into equation (5) and matching Fourier coefficients yields the relation

$$\tilde{f}_l(J_R, J_\phi) = \frac{\tilde{V}_l(J_R, J_\phi)}{l\Omega_R + m\Omega_\phi - \omega} \left(l \frac{\partial f_0}{\partial J_R} + m \frac{\partial f_0}{\partial J_\phi} \right). \quad (14)$$

The potential V_1 , and the density Σ_1 which causes it and is obtained from integrating f_1 as in equation (8), can also be expanded in position space as

$$V_1 = e^{i(m\phi - \omega t)} \sum_{j=0}^{\infty} c_j \psi_j^m(R), \quad (15)$$

$$\Sigma_1 = e^{i(m\phi - \omega t)} \sum_{j=0}^{\infty} c_j \sigma_j^m(R), \quad (16)$$

where $\psi_j^m(R)$ and $\sigma_j^m(R)$ are a complete set of real basis functions, and c_j are constant coefficients. We multiply equation (16) by $e^{i(\omega t - m\phi)} \psi_j^m(R)$ and integrate over position space to get $\sum_{k=0}^{\infty} D_{jk} c_k$, where

$$D_{jk}(m) = 2\pi \int_0^{\infty} \psi_j^m(R) \sigma_k^m(R) R dR, \quad (17)$$

are the components of a constant matrix $\mathbf{D}(m)$. It is diagonal if ψ_j^m and σ_k^m form a biorthogonal set. Alternatively, we can rewrite Σ_1 using its integral (8), and then carry out the integration over phase space using action and angle variables. This requires that we calculate Fourier coefficients of the basis potential functions

$$\Psi_{l,j}^m(J_R, J_\phi) = \frac{1}{\pi} \int_0^\pi \psi_j^m(R) \times \cos[l\theta_R + m(\theta_\phi - \phi)] d\theta_R, \quad (18)$$

$$\tilde{V}_l = \sum_{j=0}^{\infty} c_j \Psi_{l,j}^m, \quad (19)$$

(Kalnajs 1977; Tremaine & Weinberg 1984). Using equation (14) to relate the Fourier coefficients of f_1 to those of V_1 yields

$$[\mathbf{M}(m, \omega) - \mathbf{D}(m)]\mathbf{c} = \mathbf{0}, \quad (20)$$

where the components of the matrix $\mathbf{M}(m, \omega)$ are defined as

$$\frac{M_{jk}}{4\pi^2} = \sum_{l=-\infty}^{\infty} \int_0^{\infty} dJ_R \int_{-\infty}^{\infty} \frac{\left(l \frac{\partial f_0}{\partial J_R} + m \frac{\partial f_0}{\partial J_\phi} \right)}{l\Omega_R + m\Omega_\phi - \omega} \Psi_{l,j}^m \Psi_{l,k}^m dJ_\phi. \quad (21)$$

The integration is over the whole of action space [cf equation (9)], and we suppose that the integrand decays sufficiently rapidly as $J_R \rightarrow \infty$ and $J_\phi \rightarrow \pm\infty$ for the integrals to converge. This system of linear equations (20) has a non-trivial solution for the coefficient vector \mathbf{c} only if

$$\mathcal{M}(m, \omega) \equiv |\mathbf{M}(m, \omega) - \mathbf{D}(m)| = 0. \quad (22)$$

This determinantal equation defines a nonlinear eigenvalue problem for ω . Details of how to solve it are discussed in §4. Once ω is found, its eigenvector \mathbf{c} gives the physical shape of the perturbation.

2.2. Boundary Integrals

The DF of a unidirectional disk for which all the stars rotate in the prograde direction has the form

$$f_0(J_R, J_\phi) = f_0^P(J_R, J_\phi) H(J_\phi), \quad (23)$$

where H is the Heaviside function. The derivative of this DF with respect to J_ϕ is

$$\frac{\partial f_0}{\partial J_\phi} = \frac{\partial f_0^P}{\partial J_\phi} H(J_\phi) + f_0^P(J_R, 0) \delta(J_\phi). \quad (24)$$

The matrix $\mathbf{M}(m, \omega)$ then has two components

$$\mathbf{M}(m, \omega) = \mathbf{M}^A(m, \omega) + \mathbf{M}^B(m, \omega), \quad (25)$$

whose elements are

$$\frac{M_{jk}^A}{4\pi^2} = \sum_{l=-\infty}^{\infty} \int_0^{\infty} dJ_R \int_0^{\infty} \frac{\left(l \frac{\partial f_0^P}{\partial J_R} + m \frac{\partial f_0^P}{\partial J_\phi} \right)}{l\Omega_R + m\Omega_\phi - \omega} \Psi_{l,j}^m \Psi_{l,k}^m dJ_\phi \quad (26)$$

$$\frac{M_{jk}^B}{4\pi^2} = \sum_{l=-\infty}^{\infty} \int_0^{\infty} dJ_R \left[\frac{m f_0^P(J_R, 0) \Psi_{l,j}^m \Psi_{l,k}^m}{l\Omega_R + m\Omega_\phi - \omega} \right]_{J_\phi=0}. \quad (27)$$

Because $\Omega_\phi = \Omega_R/2$ for radial orbits, the denominator of the boundary integral (27) reduces to $-\omega$ for $l = -m/2$ when m is even. Modes with $\omega = 0$ are therefore precluded when $f_0^P(J_R, 0) \neq 0$. More generally, this special component of the boundary integral can be incorporated into an iterative scheme for computing eigenvalues, which we describe in §4.5.

The DF (23) also drops abruptly to zero at the circular orbit limit $J_R = 0$ so that one should also include an extra $H(J_R)$ factor in the DF. Differentiation of f_0 with respect to $J_R = 0$ then gives a $\delta(J_R)$. However it gives no boundary integral, regardless of the value of f_0 at $J_R = 0$. The reason is that its integrand, for which the $m f_0^P(J_R, 0)$ of equation (27) is replaced by $l f_0^P(0, J_\phi)$, vanishes at $J_R = 0$. That is because the Fourier coefficients $\Psi_{l,j}^m(0, J_\phi)$ vanish for all $l \neq 0$ because orbits with $J_R = 0$ are circular, and the remaining non-zero $l = 0$ Fourier coefficient is annulled by the factor l . Hence the simpler form (23) of the DF suffices.

The boundary integral (27) does not arise if the unperturbed DF contains no radial orbits so that $f_0^P(J_R, 0) = 0$. This is the case for the unidirectional DFs used by Zang (1976) and Evans & Read (1998a,b) because their DFs contain positive powers of $L = J_\phi$ as factors, and hence contain no radial orbits. They work with scalefree potentials which are singular as $R \rightarrow 0$, whereas ours are not. Only orbits with low angular momenta penetrate near the center of a cored potential. As Gerhard (1991) discusses for the analogous problem of spherical systems, most DFs for smooth potentials which produce finite densities in their cores tend to isotropy there and so have radial orbits. His reasoning applies to thin disks too. Only orbits with low angular momenta penetrate near the center, and the only alternative to radial orbits is a singular distribution of non-radial orbits, as when all orbits are circular. The need for radial orbits to provide a non-zero central density disappears if the density of the stellar disk drops to zero in the center, as it does with the cutouts which we discuss in §3.6.

The omission of the boundary integral terms (27) in the cases computed by Hunter (1992) invalidates his results. As we shall see in §5.1, the effect is substantial. Pichon & Cannon (1997) confirmed those results, but only because they repeated Hunter's error of neglecting the boundary integral. As we show in Appendix B, its omission means

neglecting the contributions to potential energy and angular momentum which arise from the perturbation of radial orbits.

Boundary integrals are avoided if one uses a Lagrangian instead of an Eulerian perturbation theory (Kalnajs 1977). The two forms of the theory are complementary and we show in Appendix B that the Lagrangian results relevant to this work can be derived simply from the Eulerian theory.

2.3. Angular Momentum and Energy

The perturbations to angular momentum and energy are of second order, and so their calculation requires considering the second order terms from (6). Summing the contributions from all elements in phase space gives

$$\mathcal{L} = \iint J_\phi f d\mathbf{J}d\Theta, \quad (28)$$

for the total angular momentum, and

$$\mathcal{K} = \frac{1}{2} \iint (v_R^2 + v_\phi^2) f d\mathbf{J}d\Theta, \quad (29)$$

for the total kinetic energy. To compute the gravitational energy, we must distinguish between the part V_0^D of the unperturbed gravitational potential V_0 which is due to the stars of the disk, and the remainder V_0^{ext} which is provided by some other and external source. The perturbational terms V_j , $j > 0$, of the potential all arise from the perturbed DF, and so all belong to the self-gravitational potential. The double contribution of the external potential to the gravitational energy is taken care of by writing it as

$$\mathcal{W} = \frac{1}{2} \iint (V + V_0^{\text{ext}}) f d\mathbf{J}d\Theta. \quad (30)$$

The leading corrections to these quantities due to the perturbations are of second order because all the first order terms vanish when integrated over θ_ϕ . They are

$$\mathcal{L}_2 = \iint J_\phi f_2 d\mathbf{J}d\Theta, \quad (31)$$

$$\mathcal{K}_2 = \iint (\mathcal{H}_0 - V_0) f_2 d\mathbf{J}d\Theta = \mathcal{K}_{2,1} + \mathcal{K}_{2,2}, \quad (32)$$

after using the zeroth order part of equation (4) to substitute for the velocities, and, because $V_0^{\text{ext}} = V_0 - V_0^D$,

$$\begin{aligned} \mathcal{W}_2 &= \frac{1}{2} \iint (V_2 f_0 + V_1 f_1 - V_0^D f_2 + 2V_0 f_2) d\mathbf{J}d\Theta, \\ &= \frac{1}{2} \iint f_1 V_1 d\mathbf{J}d\Theta + \iint V_0 f_2 d\mathbf{J}d\Theta, \\ &= \mathcal{W}_{2,1} + \mathcal{W}_{2,2}. \end{aligned} \quad (33)$$

The component $\mathcal{W}_{2,2} = -\mathcal{K}_{2,2}$ because their defining integrals match. The step to the second line of equation (33) uses the fact that the first and third terms on the first line cancel. This is seen by transforming the integrations to (\mathbf{x}, \mathbf{v}) space, and then using equations (2), (8) for $j = 2$, and Poisson integrals like (7) to relate potentials to densities, to express them as identical integrals of the product of the densities Σ_D and Σ_2 .

The simplest integral to calculate is that for the first component of $\mathcal{W}_{2,1}$ in equation (33). As we noted earlier,

the physical parts of our solutions are given by the real parts of our complex solutions. The real parts of f_1 and V_1 are given by the sums $\frac{1}{2}(f_1 + \bar{f}_1)$ and $\frac{1}{2}(V_1 + \bar{V}_1)$, where a bar denotes a complex conjugate. Therefore

$$\begin{aligned} \mathcal{W}_{2,1} &= \frac{1}{8} \iint (f_1 + \bar{f}_1)(V_1 + \bar{V}_1) d\mathbf{J}d\Theta, \\ &= \frac{1}{8} \iint (f_1 \bar{V}_1 + V_1 \bar{f}_1) d\mathbf{J}d\Theta, \\ &= e^{2st} \sum_{l=-\infty}^{\infty} W_{2,1}^l, \end{aligned} \quad (34)$$

where the components $W_{2,1}^l$ are defined by

$$\begin{aligned} W_{2,1}^l &= \pi^2 \int d\mathbf{J} \left(l \frac{\partial f_0}{\partial J_R} + m \frac{\partial f_0}{\partial J_\phi} \right) \\ &\quad \times \frac{[l\Omega_R + m(\Omega_\phi - \Omega_p)] |\tilde{V}_l|^2}{|l\Omega_R + m\Omega_\phi - \omega|^2}. \end{aligned} \quad (35)$$

We have used here, and will again, the fact that the only products which do not vanish on integration over θ_ϕ are those which pair a conjugate with a non-conjugate quantity.

We show in appendix A that

$$\mathcal{L}_2(t) = e^{2st} \sum_{l=-\infty}^{\infty} L_2^l, \quad \mathcal{K}_{2,1}(t) = e^{2st} \sum_{l=-\infty}^{\infty} K_{2,1}^l, \quad (36)$$

where the components of these sums are defined by the integrals

$$\begin{aligned} L_2^l &= -m\pi^2 \int d\mathbf{J} \left(l \frac{\partial f_0}{\partial J_R} + m \frac{\partial f_0}{\partial J_\phi} \right) \\ &\quad \times \frac{|\tilde{V}_l|^2}{|l\Omega_R + m\Omega_\phi - \omega|^2}, \end{aligned} \quad (37)$$

$$\begin{aligned} K_{2,1}^l &= -\pi^2 \int d\mathbf{J} \left(l \frac{\partial f_0}{\partial J_R} + m \frac{\partial f_0}{\partial J_\phi} \right) \\ &\quad \times \frac{(l\Omega_R + m\Omega_\phi) |\tilde{V}_l|^2}{|l\Omega_R + m\Omega_\phi - \omega|^2}. \end{aligned} \quad (38)$$

To each of the area integrals (35), (37) and (38) must be added the boundary integrals given by the delta function term of equation (24) for the prograde DF (23). The integrals can be combined to give the simple relation

$$K_{2,1}^l + W_{2,1}^l = \Omega_p L_2^l, \quad (39)$$

between the separate components. Although each of these components can be found directly from the first order solution, computing $\mathcal{W}_{2,2} = -\mathcal{K}_{2,2}$ requires more, as we show in Appendix A.

The second order corrections \mathcal{L}_2 and $\mathcal{W}_{2,1}$ to the angular momentum and gravitational energy have simple representations in terms of the real and imaginary parts of the matrix $\mathbf{M} = \mathbf{M}_R + i\mathbf{M}_I$. Combining equations (37) and (35) with expansion (19), we get the quadratic forms

$$\mathcal{L}_2(t) = -\frac{m}{4s} e^{2st} \bar{\mathbf{c}}^T \mathbf{M}_I \mathbf{c}, \quad (40)$$

$$\mathcal{W}_{2,1}(t) = \frac{1}{4} e^{2st} \bar{\mathbf{c}}^T \mathbf{M}_R \mathbf{c}, \quad (41)$$

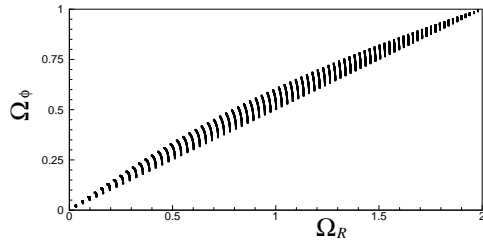


FIG. 1.— The orbital frequency space of the cored logarithmic potential (50) with frequencies in units of v_0/R_C . The lines are curves of constant E in equal steps in e^{-E} . They show that Ω_R depends only weakly on the angular momentum L , which varies from zero at their lower limit on the boundary $\Omega_\phi = 0.5\Omega_R$ which corresponds to radial orbits, to $L_c(E)$ on the curved upper limit which corresponds to circular orbits. The largest value achieved by $\Omega_i = \Omega_\phi - 0.5\Omega_R$ is 0.106. Similarly narrow lens-shaped plots are obtained for other cored potentials. When normalized to the same range of frequencies as in Fig.1, the largest value of Ω_i is 0.130 for Kuzmin's disk and 0.119 for the isochrone. Ω_R depends only on E for the isochrone, so that curves of constant E are then exactly straight.

where the superscript T denotes transposition of the column vector \mathbf{c} to generate a row vector. These expressions are real because the matrix \mathbf{M} is symmetric. Moreover multiplying equation (20) by $\bar{\mathbf{c}}^T$ and separating real and imaginary parts (\mathbf{D} is also symmetric) gives

$$\bar{\mathbf{c}}^T \mathbf{M}_{\text{RC}} \mathbf{c} = \bar{\mathbf{c}}^T \mathbf{D} \mathbf{c}, \quad \bar{\mathbf{c}}^T \mathbf{M}_{\text{RC}} \mathbf{c} = 0. \quad (42)$$

The second relation shows that $\mathcal{L}_2(t) = 0$, which it must be because the disk is not subject to any external torques, and hence its angular momentum is conserved. There is no such restriction on sizes of the separate Fourier components represented by the terms for different l in the sum (36), other than that they must sum to zero. Similarly the sizes of the different components of the potential and kinetic energy vary, because only the total energy \mathcal{E} is constrained to be zero, with $\mathcal{E}_2(t) = \mathcal{K}_2(t) + \mathcal{W}_2(t) = \Omega_p \mathcal{L}_2(t) = 0$. Hence the two components of the kinetic and potential energy are related in the same way:

$$\mathcal{K}_{2,1}(t) = -\mathcal{W}_{2,1}(t), \quad \mathcal{K}_{2,2}(t) = -\mathcal{W}_{2,2}(t). \quad (43)$$

The fact that the second order components grow twice as fast as those of first order is not paradoxical. It reflects the fact that our analysis can describe only the early stages of the growth of an instability. If we introduce a small ordering parameter ε into our expansion $f = f_0 + \varepsilon f_1 + \varepsilon^2 f_2 + \dots$ of the DF to measure the size of the perturbation relative to that of the unperturbed state, then we see that the linearization breaks down, and our analysis is unreliable, after a time t such that $\varepsilon e^{st} = O(1)$. The second order components are then of magnitude $\varepsilon^2 e^{2st}$, which is also $O(1)$. Our perturbation theory has then ceased to be valid. It is useful only when our expansion is well-ordered, that is for times for which εe^{st} is small.

2.4. Orbits and Polyachenko's Unified Theory

Every orbit in a disk with an axisymmetric potential is a rosette (Binney & Tremaine 1987). One extreme case is that of circular orbits with the maximum angular momentum $L_c(E)$ for the energy E . They have no

radial motion and their radial action $J_R = 0$. The other extreme is that of radial orbits with zero angular momentum J_ϕ . For them the polar angle ϕ remains constant, except for discontinuous changes by π whenever the orbit passes through the center. Intermediate orbits oscillate in R between maximum and minimum orbital radii R_{max} and R_{min} . Figure 1 shows an orbital frequency space for prograde orbits. Its shape is characteristic of those of other cored potentials. The upper curved boundary is formed by circular orbits for which $\Omega_\phi = V_c(R)/R$, where $V_c(R)$ is the circular velocity at radius R , and $\Omega_R = \kappa(R)$ is the epicyclic frequency. The straight lower boundary is formed by radial orbits for which $\Omega_\phi = \Omega_R/2$. The slimmness of the region in between these boundaries, where all the intermediate orbits lie, shows how limited is the range of $\Omega_\phi - \Omega_R/2$ for all orbits.

The frequency $\Omega_i = \Omega_\phi - \Omega_R/2$ and its narrow range has long been recognized as dynamically important (Lindblad 1959). Lynden-Bell (1979) pointed out that the response of an orbit to a weak bar-like potential, which rotates with a pattern speed Ω_p for which $|\Omega_p - \Omega_i|$ is small, is to align the orbit with the bar if Ω_i decreases as J_ϕ decreases when $J_f = J_R + J_\phi/2$, the action corresponding to the frequency Ω_i , is fixed. This is the case when

$$\left(\frac{\partial}{\partial J_\phi} - \frac{1}{2} \frac{\partial}{\partial J_R} \right) \Omega_i = \frac{\partial \Omega_i}{\partial L} + \Omega_i \frac{\partial \Omega_i}{\partial E} > 0. \quad (44)$$

Lynden-Bell labeled such orbits as abnormal, as opposed to normal or donkey orbits which respond contrarily to a bar-like force. It is straightforward to classify orbits in any potential according to the criterion (44); abnormal orbits are those which lie below the dashed lines in Figure 4. All sufficiently radial orbits are abnormal, but so too are all orbits which remain in the central regions of cored potentials. The dividing curve for the cored logarithmic potential in Figure 4 tends to the asymptote $L/L_c = 0.723$ as $E \rightarrow \infty$ (See §6.2). That asymptote, which is barely evident due to the compressed scale at high energies, is the dividing curve between normal and abnormal orbits for the singular logarithmic potential at all energies.

Polyachenko (2004) has outlined a unified theory of spiral and bar-like modes of disk galaxies based on Lynden-Bell's (1979) analysis. The analytical basis of his theory is a simplified version of the analysis given in §2. He uses the smallness of $|\Omega_p - \Omega_i|$ to deduce that, to leading order, the perturbed DF is given by a single $l = -m/2$ component of the Fourier series (11) so that, in our notation,

$$f_1 \simeq e^{i[m(\theta_\phi - \theta_{R/2}) - \omega t]} \tilde{f}_{-m/2}(J_R, J_\phi). \quad (45)$$

Polyachenko's equation (11) relates the perturbed DF to its potential when averaged over the 'fast' angle θ_R . That averaged potential is given in our notation by the single $l = -m/2$ component of the Fourier series (12). Polyachenko's equation (11) is therefore equivalent to the relation

$$(m\Omega_i - \omega) \tilde{f}_{-m/2} = m \left(\frac{\partial f_0}{\partial J_\phi} - \frac{1}{2} \frac{\partial f_0}{\partial J_R} \right) \tilde{V}_{-m/2}. \quad (46)$$

He has a different method for solving his equation (11) which has the advantage that he is able to derive a linear eigenvalue problem for ω , albeit one which must be

solved for an unknown function of the two action variables. Equation (46) shows that his method is equivalent to the Kalnajs matrix formulation when that formulation is simplified by replacing the sum over l in the coefficient equation (21) by the single $l = -m/2$ term, or just the $l = -1$ term in the important $m = 2$ case. Hence the matrix method can be applied to check the accuracy and validity of Polyachenko's approximations by comparing its results with those obtained when only the $l = -1$ terms of the matrix $\mathbf{M}(2, \omega)$ are used. Such comparisons are made throughout §5, and discussed in §6.2.

3. MODELS FOR GALACTIC DISKS

In §3.1, §3.2, and §3.3 we give the three potentials which we use for stability calculations; Kuzmin's disk, the isochrone, and the cored logarithmic potential (Kuzmin 1956, Binney & Tremaine 1987). The rotation curves for both Kuzmin's disk and the isochrone rises at small radii, peaks at a characteristic radius, and then falls like a Keplerian potential at large distances. That for the cored logarithmic potential gives a flat rotation curve at large distances. All potentials have smooth cores. In §3.4 we discuss constraints on the sizes of exponential stellar disks which lie in cored logarithmic potentials. In §3.5 we construct DFs for such stellar disks. In §3.6 we discuss cutout functions which can be applied to DFs to model hot central bulges.

3.1. Kuzmin's Disk

Kuzmin's disk is known also as the Kuzmin-Toomre disk because it is Model 1 of a family given by Toomre (1963). Its potential and self-consistent density are

$$V_0(R) = \frac{-GM}{\sqrt{R^2 + R_C^2}}, \quad \Sigma_0(R) = \frac{MR_C}{2\pi(R^2 + R_C^2)^{3/2}}, \quad (47)$$

where R_C is the core radius of the potential. Kuzmin's disk has been widely used for stability studies because of its simplicity. Sellwood & Athanassoula (1986) and Athanassoula & Sellwood (1986) used it for N -body simulations, while Hunter (1992), Pichon & Cannon (1997) and Polyachenko (2004) have used it for analyses based on the collisionless Boltzmann equation. To have results which can be compared with those of earlier work, we use the DFs given by Miyamoto (1971) and those used in Athanassoula & Sellwood's simulations.

3.2. The Isochrone Disk

The potential and self-consistent density of the isochrone disk are

$$V_0(R) = \frac{-GM}{R_C + \sqrt{R^2 + R_C^2}}, \quad (48)$$

$$\Sigma_0(R) = \frac{MR_C}{2\pi R^3} \left[\ln \left(\frac{R + \sqrt{R^2 + R_C^2}}{R_C} \right) - \frac{R}{\sqrt{R^2 + R_C^2}} \right] \quad (49)$$

Again R_C is the core radius of the potential. We use the DFs given in Kalnajs (1976b), modified so as to allow for a population of retrograde stars in the manner specified in Earn & Sellwood (1995). The stability of these models was investigated by Kalnajs (1978), Earn & Sellwood (1995) and Pichon & Cannon (1997).

3.3. The Cored Logarithmic Potential

The cored logarithmic potential, which has been widely used in galactic studies because of its flat rotation curve, is

$$V_0(R) = v_0^2 \ln \sqrt{1 + R^2/R_C^2}, \quad (50)$$

where v_0 is the flat rotation velocity, and R_C is again the core radius. The disk density needed to produce the potential (50) is

$$\Sigma_0(R) = \frac{v_0^2}{2\pi G \sqrt{R^2 + R_C^2}} E \left(\frac{R^2}{R^2 + R_C^2} \right), \quad (51)$$

where E is the complete elliptic integral of the second kind. This self-consistent density may be derived by Toomre's (1963) Bessel function method, using in turn formulas (6.566.2), (6.576.3), (9.131.1), and (8.114.1) of Gradshteyn & Ryzhik (1980, hereafter GR). It can also be obtained by taking the $\beta \rightarrow 0$ limit in equations (4.7) of Qian (1992) for $m = 0$ and $\gamma_1 = 0.5$. The limit is straightforward for the density, but it is necessary first to subtract the constant value of the potential at $R = 0$ before taking the $\beta \rightarrow 0$ limit for the potential.

The potential-density pair (50) and (51) is similar to that of the Rybicki disk (Zang 1976; Evans & Collett 1993) for which

$$V_0(R) = v_0^2 \ln \left(1 + \sqrt{1 + R^2/R_C^2} \right), \quad (52)$$

$$\Sigma_0(R) = \frac{v_0^2}{2\pi G \sqrt{R^2 + R_C^2}}. \quad (53)$$

Rybicki's disk is obtained by subtracting Toomre's (1963) Model 0 from a singular Mestel (1963) disk. The density (51) for the cored logarithmic potential is larger than that of the Rybicki disk in the center, which is why it has somewhat larger circular velocities. Both disks resemble the singular Mestel disk, whose stability has been studied by Zang (1976) and Evans & Read (1998a,b), at large distances. Both tend to that singular limit as the core radius $R_C \rightarrow 0$.

3.4. Exponential Disks in the Cored Logarithmic Potential

It is widely accepted that the densities of the stellar disks of spiral galaxies decay exponentially with distance (Freeman 1970). We study cored disks with densities of the form

$$\Sigma_D(R) = \Sigma_s \exp \left[-\frac{\sqrt{R^2 + R_C^2}}{R_D} \right], \quad (54)$$

where R_D is the length-scale of the exponential decay, and Σ_s is a density scale. We include the core radius R_C of the potential in the density (54) to avoid the logarithmic singularity of the uncored exponential disk $\Sigma_D = \Sigma_s \exp(-R/R_D)$ (Freeman 1970). Vauterin & Dejonghe (1996) did likewise.

The self-gravitational potential due to the cored disk density (54) can be derived by the method of Evans & de Zeeuw (1992) as

$$V_0^D(R) = -2\pi G \Sigma_s R_D \times \int_0^\infty \frac{x^2 J_1(x) dx}{\sqrt{x^2 + \lambda^2} \sqrt{x^2 + \lambda^2 + R^2/R_D^2}}. \quad (55)$$

Here $\lambda = R_C/R_D$ and J_1 is the Bessel function of the first kind. Beware that this integral must be evaluated with great care because it is oscillatory and its amplitude decays only as $x^{-1/2}$ as $x \rightarrow \infty$. $V_0^D(R)$ reduces to the potential of the exponential disk in the limit of $R_C \rightarrow 0$ when $\lambda \rightarrow 0$.

There are limits on the scales of a cored exponential disk (54) lying in the cored logarithmic potential (50). The difference $[V_0(R) - V_0^D(R)]$ between the total potential and that of the disk must be provided by some halo or bulge component of the galaxy, whose density must be everywhere positive. If that halo/bulge is spherical, then its density is given by Poisson's equation as

$$\rho_H(r) = \frac{1}{4\pi G} \frac{1}{r^2} \frac{d}{dr} [rv_H^2(r)], \quad (56)$$

$$v_H^2(R) = R \left[\frac{dV_0(R)}{dR} - \frac{dV_0^D(R)}{dR} \right] \geq 0, \quad (57)$$

(Zang 1976; Vauterin & Dejonghe 1996) where $r = \sqrt{R^2 + z^2}$. Here $v_H^2(R)$ gives the amount by which the square of the circular velocity for the galaxy exceeds that of the disk alone. The physically necessary condition that $\rho_H(r) > 0$ requires that $v_H^2(R) > 0$, but is more restrictive. The region below the solid curve in Figure 2 gives the range of the dimensionless combinations of parameters $G\Sigma_s R_D/v_0^2$ and R_C/R_D which it allows. The boundary value $G\Sigma_s R_D/v_0^2 = 0.304$ of the solid curve at $\lambda = 0$ applies to the limit of the uncored exponential disk in a singular logarithmic potential. An alternative statement of the condition $\rho_H(r) > 0$ in this limit is $v_0(R_D/GM_D)^{1/2} > .723$, where M_D is the mass of the uncored exponential disk.

Sellwood (1989), and unpublished work by Toomre described there, studied modes of the uncored exponential disk in the cored logarithmic potential (50). The critical value of $v_0(R_D/GM_D)^{1/2}$ needed to ensure that $\rho_H > 0$ for this case is not greatly changed when the logarithmic potential is cored. It is reduced only to 0.691 when $\lambda = R_C/R_D = 0.5$. For $\lambda = 0.2$ and $v_0(R_D/GM_D)^{1/2} = 0.6$ as in the model displayed in Sellwood's Figures 1 and 2, not only does ρ_H become negative, but $v_H^2(R) < 0$ for $1.4 < R/R_D < 3.0$. The fixed halo therefore exerts an outward force in this range. (The singular nature of the potential of the uncored exponential disk also causes $\rho_H < 0$, but only for $R/R_D \ll 1$ which is well below the softening length used in computations.)

Giovanelli & Haynes (2002) analyzed a large number of rotation curves and have found that the ratio of the scale length of the steep inner rise of the rotation curve to the scale length of the exponential varies from 0.63 for the most luminous galaxies, to 1.28 for their least luminous. They fit a parametric model in which the rotation curve decays exponentially towards its form in the outer regions, and hence their ratios provide only the approximate guidance that it is to reasonable to use values of order unity for our ratio R_C/R_D . Figure 3 plots total circular velocity, and the parts provided by the disk and the halo/bulge for three different relative sizes of the exponential disk which more than cover their range. The value of $G\Sigma_s R_D/v_0^2$ is close to 90% of the maximum allowable for that R_C/R_D in each case. The least extensive disk makes the largest contribution to the ro-

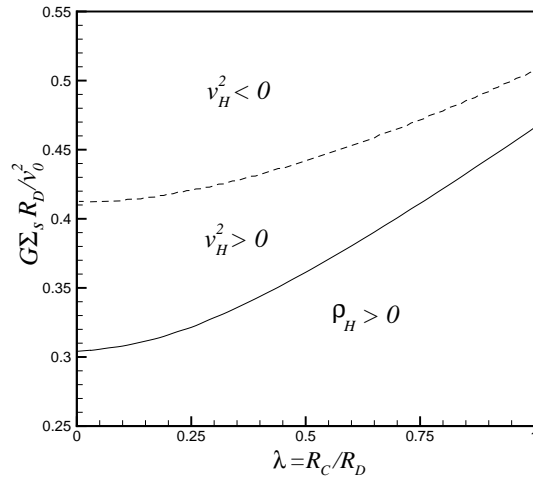


FIG. 2.— The boundary of physical exponential disks (solid line) in the parameter space. Models below the solid line have spherical halos with $\rho_H > 0$ at all radii.

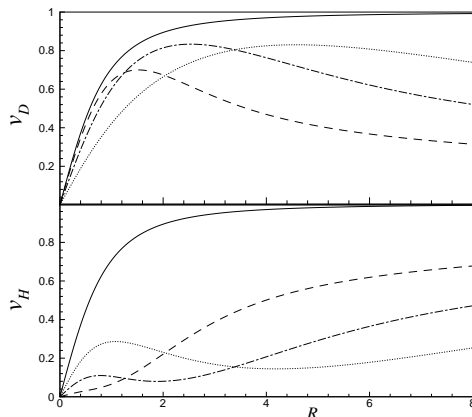


FIG. 3.— The rotational velocities due to the disk (upper panel) and halo/bulge (lower panel) components of the exponential disk, in units in which $R_C = v_0 = 1$. In each case the dashed, dot-dashed, and dotted lines correspond to $(R_D, G\Sigma_s R_D) = (0.5, 0.6)$, $(1, 0.42)$ and $(2, 0.32)$, respectively, while the solid line shows the circular velocity of the cored logarithmic potential.

tation curve at the center, but its relative contribution then declines rapidly. The disk's contribution tracks the rotation curve considerably further in the intermediate case with $R_D = R_C$, and requires only a relatively small contribution from a central halo/bulge to make up the deficit. As R_D increases, the disk becomes less maximal and an increasingly large spherical central halo/bulge is needed.

3.5. Distribution Functions for the Exponential Disk

We construct DFs by using the identity

$$e^{-\Phi} \sqrt{1 + \frac{R^2}{R_C^2}} = 1, \quad \Phi = \frac{V_0}{v_0^2}, \quad (58)$$

to partition the density (54) in the form

$$\Sigma_D(R) = \Sigma_s e^{-\lambda e^\Phi} e^{-2N\Phi} \left(1 + \frac{R^2}{R_C^2}\right)^N, \quad \lambda = \frac{R_C}{R_D}. \quad (59)$$

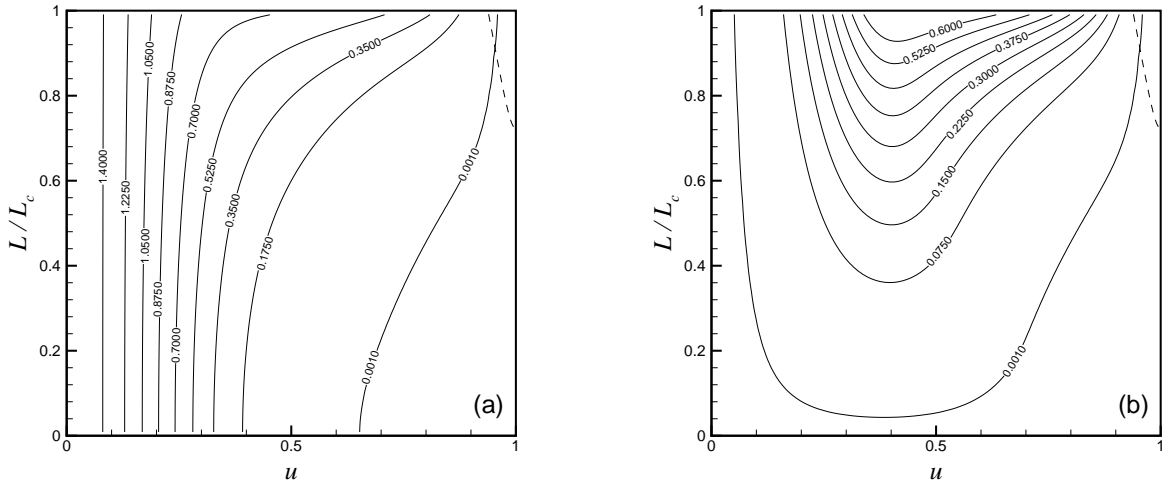


FIG. 4.— (a) The DF f_0^P of the exponential disk for $N = 6$ and $R_C = R_D = 1$, and (b) that DF after applying the cutout (63) with $L_0 = 0.1$. The abscissa $u = \sqrt{1 - e^{-E}}$ is that used in numerical work, as defined in equation (67). It ranges from $u = 0$ at the center to $u = 1$ at infinite distances. Contours are labeled in units of Σ_s , and show slopes which increase with increasing N . The dashed line shows the curve $\partial\Omega_i/\partial L + \Omega_i\partial\Omega_i/\partial E = 0$. Only orbits which lie above this curve are normal in Lynden-Bell's (1979) classification.

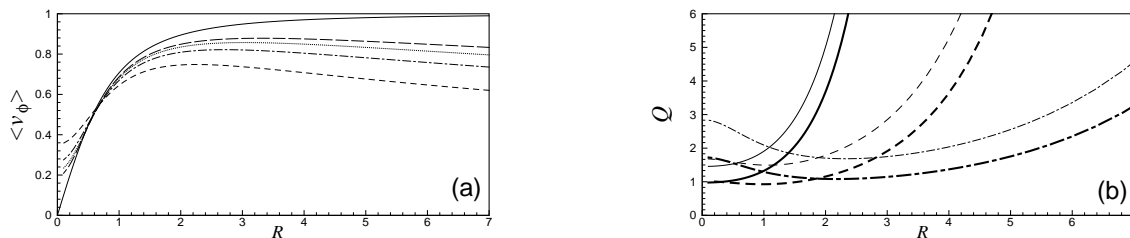


FIG. 5.— (a) Circular velocity (solid line) and mean rotation velocities of the exponential disk. Dashed, dot-dashed, dotted and long-dashed lines respectively show the mean rotation velocity $\langle v_\phi \rangle$ of exponential disks with $N = 2, 4, 6$ and 8 . All curves are for $R_C = R_D = v_0 = 1$. (b) Toomre's Q for the exponential disk for $R_C = 1$ with $N = 2$ (thin lines) and $N = 6$ (thick lines). Solid, dashed and dot-dashed lines here correspond to $(R_D, G\Sigma_s R_D) = (0.5, 0.6), (1, 0.42)$ and $(2, 0.32)$, respectively as in Figure 3.

Here N is an integer parameter which allows us to generate a family of models. Binomial expansion of $(1 + R^2/R_C^2)^N$ gives Σ_D as a sum of powers of R^2 multiplied by functions of the potential Φ . We then use Sawamura's (1988) method, following Evans & Collett (1993) §3.1, to find the DF as the series

$$f_0^P(E, L) = \Sigma_s \sum_{n=0}^N \binom{N}{n} \left(\frac{L}{R_C}\right)^{2n} g_n(E), \quad (60)$$

where the functions $g_n(E)$ are given by

$$g_n(E) = \frac{(-1)^{n+1}}{2^n \sqrt{\pi} \Gamma(n + 1/2)} \times \frac{d^{n+1}}{dE^{n+1}} \left(e^{-2NE/v_0^2} e^{-\lambda e^{E/v_0^2}} \right). \quad (61)$$

Figure 4a plots an $N = 6$ case of equation (60).

Figure 5a plots the mean rotation velocity $\langle v_\phi \rangle$ for four different values of N , and shows that the disks become increasingly cool and centrifugally supported with increasing N . The mean rotation velocity exceeds the circular velocity near the center, due to the $n = 0$ isotropic term in the DF (60). Its density, which is

$$\Sigma_{\text{iso}} = \Sigma_s \left(1 + \frac{R^2}{R_C^2}\right)^{-N} \exp\left[-\frac{\sqrt{R^2 + R_C^2}}{R_D}\right], \quad (62)$$

is confined to the central region. It is compressed as N increases, and disappears as $N \rightarrow \infty$ along with all radial orbits. The other interesting feature of Figure 5a is that $\langle v_\phi \rangle$ declines away from v_0 at large distances. Evans & Collett's (1993) models for a simple uncored exponential disk in a singular logarithmic potential have the same property - see their Figure 2a - and for the same reason. Although $\langle v_\phi \rangle \rightarrow v_0$ as $N \rightarrow \infty$, their equation (3.17) also shows that $\langle v_\phi \rangle$ decreases for increasing R for fixed N , as in their Figure 2a and our Figure 5b.

Figure 5b plots the Toomre stability parameter Q for two different N values and for the same three sizes of the exponential disk as in Figure 3. The cooler $N = 6$ models have regions of varying extent in which Q is close to its marginal value of 1. The growth of Q with increasing R is due primarily to decreasing Σ_D because the radial velocity dispersion $\sigma_R = \sqrt{\langle v_R^2 \rangle}$ falls off only mildly.

3.6. Simulating a Hot Bulge

Most spiral galaxies of S type have a three-dimensional central bulge which stands out from the disk. Kormendy (1977) proposed modeling the disk with an inner-truncated exponential so that the disk has a hole in its center, and others have followed. We construct disks with central holes by removing stars which penetrate to

the center. We use a cutout function $H_{\text{cut}}(L)$ to change an unperturbed DF $f_0(E, L)$ to $H_{\text{cut}}(L)f_0(E, L)$. In so doing, we make the tacit assumption that the part of the gravitational potential which the cutout stars had previously provided, is instead provided by a bulge which is so hot that it does not respond at all to disturbances in the disk.

Cutouts were introduced first in Zang's (1976) pioneering study of DFs in a singular scalefree logarithmic potential. His purpose was to eliminate stars with short dynamical time scales and high dynamical frequencies. Dynamical frequencies in cored potentials are bounded (cf Figure 1) and so avoid that problem. Zang's cutout also removes stars on nearly radial orbits, regardless of their dynamical frequencies. Evans & Read (1998a) went further and also used an outer cutout to remove stars that spend so much time far out in the disk that they do not respond to its changing potential. Their disks are infinitely massive whereas ours are not; ours have sufficiently few such stars that they do not pose a problem.

We apply a cutout function

$$H_{\text{cut}}(L) = 1 - e^{-(L/L_0)^2}, \quad (63)$$

where L_0 is some angular momentum scale. Like Zang's, it removes stars for which L is significantly less than L_0 , but has no effect on stars with $L \gg L_0$. It also removes stars on radial and near-radial orbits, as well as stars of low energy because they too have low angular momenta. The result of the cutout (63) is to give an active surface density

$$\Sigma_{\text{act}} = \int H_{\text{cut}}(L)f_0(E, L)d\mathbf{v}, \quad (64)$$

which tends to zero at the center, and hence models a central hole. Figure 4b shows the effect of an $L_0 = 0.1$ cutout on the DF of Figure 4a. No boundary integrals (27) arise for such cutout unidirectional disks because their unperturbed DF vanishes at $L = 0$. The active surface density corresponding to the cutout DF of Figure 4b is shown in Figure 14c. It shows that our truncation is far less sharp than that given by Kormendy's (1977) inner-truncated exponential formula.

4. COMPUTATIONAL PROCEDURES

This section gives details on the numerical methods and algorithms we used. Those uninterested in these topics should skip to §5 where we present the results of our computations.

4.1. Choice of Basis Functions

We use the set of basis functions introduced by Clutton-Brock (1972), and simplified by Aoki & Iye (1978), to relate densities and potentials. They are

$$\psi_j^m = -\frac{1}{(1 + R^2/b^2)^{1/2}} P_{m+j}^m(\xi), \quad (65)$$

$$\sigma_j^m = \frac{(2m + 2j + 1)}{2\pi Gb(1 + R^2/b^2)^{3/2}} P_{m+j}^m(\xi), \quad (66)$$

where $\xi = (R^2 - b^2)/(R^2 + b^2)$ and the $P_{m+j}^m(\xi)$ are associated Legendre functions. The variable ξ ranges from -1 at $R = 0$ to 1 as $R \rightarrow \infty$. The functions (65) and (66) form a complete biorthogonal set over the range $0 \leq R < \infty$, and so are useful for disks of infinite extent.

The parameter b is a length scale which can be chosen so as to match the oscillatory behavior of the Legendre functions with the regions in which modes vary most. We have found that repeating calculations with different b values provides a helpful check on their accuracy.

The Clutton-Brock functions with the choice $b = R_C$ are a simple choice to use with Kuzmin's disk. The self-consistent potential-density pair (47) is then given by $(V_0, \Sigma_0) = (GM/R_C)(\psi_0^0, \sigma_0^0)$. However we have also found Clutton-Brock functions to work well for determining the modes of the exponential disk (54), even though its density decays more rapidly than the R^{-3} decay of the σ_j^0 functions. This seems to be because modes decay rapidly in the outer regions and are little influenced by matter there. For instance, the frequencies which Pichon & Cannon (1997) computed for a Kuzmin's disk truncated at $R = 5R_C$ differ little from those computed by Hunter (1992) who did not truncate them. Unfortunately, the Clutton-Brock functions are not suitable for computing reliable values of the gravitational energy component $\mathcal{W}_{2,2}$ using the sum (A18). The reason is that the combination of the growth of the logarithmic potential V_0 at large R with the R^{-3} decay of the σ_j^0 causes the integrals in that sum to grow slowly with increasing j . The convergence of the sum is poor, and we do not have accurate values for $\mathcal{W}_{2,2}$. No such problem arises with the more rapidly decaying potentials of the Kuzmin and isochrone disks.

Kalnajs (1976a) gave a set of biorthogonal Abel-Jacobi functions which are suitable for disks of finite radius, and were used by Earn & Sellwood (1995) and Pichon & Cannon (1997). No recursive relations have been given for them, and so they must be computed using explicit formulae. That requires high-precision arithmetic because of cancellations between large coefficients of opposite sign. Clutton-Brock functions are computed accurately using simple recursive formulae, and do not need high-precision arithmetic.

4.2. Action Space Integrations

Since DFs are usually given in terms of the energy E and the angular momentum L , it is more convenient to use E and L as the integration variables for integrations over action space. We do this and replace the Jacobian $dJ_R dJ_\phi$ with $dE dL/\Omega_R$. To evaluate the surface integral in the (E, L) -space, we adopt the trapezoidal rule in the E -direction and an extended open scheme [equation (4.1.18) of Press et al. (1992)] in the L -direction. With this latter choice, we avoid the circular and radial orbit boundaries where the calculation of orbital frequencies and their derivatives with respect to the actions has some computational difficulties. The Fourier coefficients $\Psi_{l,j}^m$, and hence the integrands, all vanish at E_{min} and E_{max} because the potential functions $\psi_j^m(R)$ vanish at $R = 0$ (for $m > 0$) and as $R \rightarrow \infty$. For the exponential disk for which $0 \leq E < \infty$, we transform from E to u where

$$E = -\ln(1 - u^2), \quad (67)$$

and map $0 \leq E < \infty$ onto the finite range $0 \leq u < 1$. We generate a uniform $n_G \times m_G$ mesh in either $(E, L/L_c)$ -space or $(u, L/L_c)$ -space, and evaluate integrands at grid points.

Accurate evaluation of the boundary integrals \mathbf{M}^B requires an especially careful treatment of the central region, especially for centrally concentrated modes. More basis functions are needed there, up to 15 in some cases, and a fine grid to allow for the oscillations of Fourier coefficients near the center where f_0^P is largest. We use a uniform grid in $u = \sqrt{1+E}$ for boundary integrals for Kuzmin's disk; the transformation (67) still works well for the exponential disk.

Formulas for the orbital frequencies Ω_R and Ω_ϕ defined in (10) are obtained by differentiating equation (9). Computationally convenient forms of the integrals which occur in them are given by Evans & Read (1998a). An alternative and compact form is obtained by expressing E and L in terms of the maximum and minimum orbital radii, R_{\max} and R_{\min} . Then if we define $x = R^2$ and $U(x) = 2R^2V_0(R)$, we get

$$2R^2(E - V_0) - L^2 = (x_{\max} - x)(x - x_{\min})U[x_{\min}, x, x_{\max}]. \quad (68)$$

Here $U[x_{\min}, x, x_{\max}]$ denotes a second order divided difference, as in de Zeeuw & Hunter (1990). Using this result, and then the substitution $x = x_{\min} \cos^2 \varphi + x_{\max} \sin^2 \varphi$, the orbital frequencies are given by

$$\Omega_R(J_R, J_\phi) = \frac{\pi}{I_0}, \quad \Omega_\phi(J_R, J_\phi) = \frac{J_\phi I_1}{I_0}, \quad (69)$$

where

$$I_k = \int_0^{\pi/2} \frac{d\varphi}{x^k \sqrt{U[x_{\min}, x, x_{\max}]}}. \quad (70)$$

These integrals are free of singularities, and they can be differentiated analytically with respect to E and L to obtain the derivatives of the frequencies needed in §2.4.

4.3. Fourier Coefficients

We use the trapezoidal rule to evaluate the Fourier coefficients (18) because it is a highly accurate method for integrating periodic functions if a fine enough gridding is used (e.g., Davis & Rabinowitz 1984). Closed form expressions for $R(t)$ and $\phi(t)$ are known for orbits in the planar isochrone (Boccaletti & Pucacco 1996). Otherwise orbits must be obtained by numerical integration. We integrate the equations of motion for a half period, starting from the initial conditions $t = \theta_R = \theta_\phi = v_R = \phi = 0$, $R = R_{\min}$, and record the values at equal steps in θ_R for use with the trapezoidal rule.

4.4. Evaluating Matrix Elements

The denominator term $(l\Omega_R + m\Omega_\phi - \omega)$ in the integrals (21) for the matrix elements M_{jk} may vanish if ω becomes real during the course of the iterative search. When it does, the integral becomes singular. We use Hunter's (2002) method to handle such resonances. It is designed to ensure that matrix elements are calculated according to Landau's (1946) rule, and also provides an efficient way for the repeated evaluations of the matrix elements needed in an iterative search for eigenvalues. It requires the evaluation of the integrals

$$\alpha_n(j, k, l) = \frac{4(2n+1)\pi^2}{(\eta_{\max} - \eta_{\min})} \iint \left[l \frac{\partial f_0}{\partial J_R} + m \frac{\partial f_0}{\partial J_\phi} \right] \times \Psi_{j,l}^m \Psi_{k,l}^m P_n[w(l)] dJ_R dJ_\phi, \quad (71)$$

where $\eta = l\Omega_R + m\Omega_\phi$ and $w(l) = 2(\eta - \eta_{\min})/(\eta_{\max} - \eta_{\min}) - 1$. The extreme values of η depend on l as is seen from Figure 1. Matrix elements are then formed as sums

$$M_{jk}(m, \omega) = \sum_{l=-\infty}^{\infty} \left\{ -2 \sum_{n=0}^{\infty} \alpha_n(j, k, l) Q_n[\lambda(l)] \right\}. \quad (72)$$

where $\lambda(l) = 2(\omega - \eta_{\min})/(\eta_{\max} - \eta_{\min}) - 1$. Beware that the sign of the matrix \mathbf{M} used here is the opposite of that in Hunter (2002). Both P_n and Q_n denote the usual Legendre functions. The multivalued Q_n functions must be evaluated for real ω by taking the limit $s = \text{Im}(\omega) \rightarrow 0$ through positive values. The coefficients α are computed and stored for the whole ranges of n , j , k and l . Weinberg (1994) gives an alternative method of handling resonances.

4.5. Searching for Eigenvalues

We search for eigenvalues ω using the modified Newton method of Stoer & Bulirsch [1993, eq. (5.4.1.7)]. We calculate $\mathcal{M}(m, \omega)$ using an LU decomposition as in Press et al. (1992). We compute the derivative $d\mathcal{M}/d\omega$, needed by Newton's method, numerically using central differences. Whether Newton's method converges or not, and the rapidity with which it converges if it does, depends on the choice ω_0 of a starting approximation. We are most interested in finding the modes with the largest growth rates. The set of all initial guesses of ω_0 which lead to an eigenvalue is the basin of attraction of its mode. Our computations show that the ω_0 -space is dominated by the basin of attraction of the fastest growing mode, but that there are also regions which lead to other modes. We have found two modes for most of our models.

We have found the following search procedure to be useful when there are large boundary integral terms. As we noted in §2.2, the $l = -1$ component of the boundary integral \mathbf{M}^B of (27) is

$$-\frac{4\pi^2}{\omega} \int_0^\infty dJ_R [2f_0^P \Psi_{-1,j}^2 \Psi_{-1,k}^2]_{J_\phi=0} = -\frac{1}{\omega} A_{jk}, \quad (73)$$

where A_{jk} are the components of a positive definite matrix \mathbf{A} which is independent of ω . We define the matrices \mathbf{B} and \mathbf{E} as

$$\mathbf{B} = \mathbf{M} + \frac{1}{\omega} \mathbf{A}, \quad \mathbf{E} = \mathbf{A}^{-1} \cdot (\mathbf{B} - \mathbf{D}). \quad (74)$$

The eigenvalue problem (20) can be recast as

$$\left(\mathbf{E} - \frac{1}{\omega} \mathbf{I} \right) \mathbf{c} = \mathbf{0}, \quad (75)$$

so that $1/\omega$ is an eigenvalue of ω -dependent matrix \mathbf{E} . We find that it is simple to find roots of the reduced equation $|\mathbf{E}| = 0$ by Newton's method because they are insensitive to the initial choice of ω . We use a continuation scheme to find eigenvalues of the recast eigenvalue problem (75) by introducing a parameter μ and defining a sequence of problems

$$\left| \mathbf{E}(m, \omega) - \frac{\mu}{\omega} \mathbf{I} \right| = 0. \quad (76)$$

We proceed by continuation in μ from the simple $\mu = 0$ case to the $\mu = 1$ case of equation (75), using our solutions at one stage as the initial estimate for the solution

at the next stage. We also apply continuation methods when we use eigenvalue estimates obtained from matrix truncations of one size as initial estimates for larger matrix truncations.

Getting a converged solution needs some controls on our series truncations and integration grids. Using a fine grid at the energies corresponding to distant stars, requires too many Fourier coefficients to expand the basis functions. In turn, a large l_{\max} ($|l_{\min}|$) increases the cost of computations while such an attempt does not capture further physics of the problem. In fact, unstable waves are confined to the central regions of stellar disks and they lose much of their power as they reach the corotation and outer Lindblad resonances. So, large-amplitude orbits, which spend much time in outer regions, do not respond to density perturbations. This is the reason why outer-truncated disks have been used successfully by others (Athanasoula & Sellwood 1986, Pichon & Cannon 1997). We allow disks to be infinite. We start the computation of ω with 40×40 grids and $j_{\max} = 2$. We simultaneously increase j_{\max} and grid size until the relative accuracy in computing ω becomes better than 5×10^{-3} . We find in most cases that this accuracy is achieved when $n_G \approx 75$ and $j_{\max} = 10$. An independent check of accuracy is to see whether the condition $e^{-2st}\Omega_p\mathcal{L}_2 = 0$ is satisfied after finding ω and \mathbf{c} . In all of our unstable models, the normalized value of this quantity remains below 5×10^{-3} .

After an eigenvalue ω has been found, we need its eigenvector \mathbf{c} . A theorem of linear algebra states that, when ω is an eigenvalue, then any column of the adjoint matrix $\text{adj}[\mathbf{M}(m, \omega) - \mathbf{D}(m)]$ is an eigenvector associated with ω (Brogan 1990). The computation of the adjoint matrix requires the computation of the minor determinants of $\mathbf{M}(m, \omega) - \mathbf{D}(m)$. It can be done rapidly and accurately because we work with matrices of relatively small size.

5. M=2 MODES OF DISKS

The following three subsections present our numerical results for the different DFs we have studied. Properties of $m = 2$ modes are listed in the tables, and selected ones are displayed. The final column in each table gives the pattern speed Ω_p computed by Polyachenko's simplified theory described in §2.4. No growth rate s is listed for this case because it is always 0.

We have found two modes for most of the models we have investigated. Classifying them is less straightforward than it is for simpler physical systems, for which the fundamental mode has the lowest frequency and simplest structure, and modes of successively higher order have higher frequencies and more complex structure. The most important instability is that with the highest growth rate. Often it also has the simplest structure. However, we find that small changes in the orbital population have a much greater effect on relative growth rates than they do on radial structure, with the result that the mode with the simplest structure is not always the fastest growing. For that reason we have chosen structure, rather than growth rate, as our criterion for determining which modes are fundamental. Fundamental modes are labeled 1 and secondary modes 2 in our tables.

The displays include a contour plot of the perturbed

density

$$\Sigma_1 = P(R) \cos [2\phi - \omega t + \vartheta(R)]. \quad (77)$$

It is obtained from the real part of equation (16) after writing its R -dependent part in the form $P(R)e^{i\vartheta(R)}$ for some real functions $P(R)$ and $\vartheta(R)$. Eigenvectors are arbitrary to within a complex constant multiple, with the result that the phase $\vartheta(R)$ is arbitrary to within an additive constant, so that modes are oriented arbitrarily. As usual, we draw only the contours for positive levels of the perturbed density (77); those for negative levels have exactly the same pattern, rotated by 90° and occupy the blank sectors. The levels of the contours are in steps of 10% of the maximum of Σ_1 from 10% to 90%. The length scale of all plots is that of the core radius of the potential, so that $R_C = 1$.

Solid and dotted circles on the contour plots of a wave pattern mark the radii R_{CR} and R_{OLR} of circular orbits in co-rotation resonance (CR) and outer Lindblad resonance (OLR) respectively with a neutral $s = 0$ mode with the pattern speed Ω_p of that mode. All pattern speeds are too large for there to be an inner Lindblad resonance (ILR). Orbits of any shape, not just circular ones, may be resonant. For example, the orbits which are in a CR with a pattern speed Ω_p are those which lie on the horizontal line $\Omega_\phi = \Omega_p$ which cuts through the lens-shaped region of Figure 1 from the circular orbit boundary on its left to the radial orbit boundary on its right. These orbits are spread out in space and not confined to one specific circle. They are more concentrated near that circle when most orbits are near-circular, but not otherwise. Similarly the orbits in an OLR are those for which $\Omega_\phi = \Omega_p - \Omega_R/2$, and lie on a line through Figure 1 with slope $-1/2$. They too range from circular to radial. They have lower orbital frequencies than those in the CR because they lie further out in the disk. An ILR occurs only for the limited range of Ω_p values for which the line $\Omega_\phi = \Omega_p + \Omega_R/2$ of slope $1/2$ intersects the lens-shaped region of Figure 1. When this happens, there are two circular orbits, as well as a generally wide range of intermediate orbits, in ILR. For the most part we find unstable modes with growth rates $s > 0$. They have no resonances, only near-resonances at which the denominators of the matrix components (21) are small when s is small.

Below each contour plot is a plot of the radial variations of the amplitude $P(R)$ of the perturbed density (full curve) and of the unperturbed density (dashed curve). Below this is a bar chart which displays the values of the different Fourier components $L_{2,1}^l$, $K_{2,1}^l$ and $W_{2,1}^l$ computed for them. The values of all these components depend on how the eigenvector \mathbf{c} is normalized. We normalize \mathbf{c} so as to make the positive and negative components of $e^{-2st}\Omega_p\mathcal{L}_2$ sum to ± 1 respectively. We find that $\mathcal{K}_{2,1}$ is always positive. This does not necessarily imply that all modes release gravitational energy and convert it to kinetic energy. Such a release occurs only if the sum of the two components $\mathcal{K}_{2,1} + \mathcal{K}_{2,2}$ is positive. Our tables for Kuzmin and isochrone disks list values of the ratio $\mathcal{K}_{2,2}/\mathcal{K}_{2,1}$ for each mode. A mode converts gravitational energy to kinetic energy if this ratio exceeds -1, and vice versa if the ratio is less than -1. There is no conversion if the ratio is exactly -1.

TABLE 1. EIGENVALUES FOR $m = 2$ MODES OF UNIDIRECTIONAL MIYAMOTO MODELS FOR KUZMIN'S DISK.

n_M	L_0	M_{act}	mode	Full Model					$l = -1$ only	
				Ω_p	s	$\mathcal{K}_{2,2}/\mathcal{K}_{2,1}$	R_{CR}	R_{OLR}	Ω_p	
3	0	1.000	1	0.825	0.939	1.58	0.541	1.296	0.649	
3	0	1.000	2	0.418	0.265	1.88	1.483	2.246	0.270	
5	0	1.000	1	0.913	1.216	1.61	0.359	1.176	0.738	
5	0	1.000	2	0.530	0.409	1.86	1.154	1.878	0.323	
7	0	1.000	1	0.963	1.465	2.58	0.227	1.115	0.805	
7	0	1.000	2	0.643	0.588	2.64	0.895	1.609	0.372	
3	0.2	0.868	1	1.023	0.114	-3.26	...	1.045	...	
3	0.2	0.868	2	0.336	0.203	-1.67	1.811	2.632	0.259	
5	0.2	0.882	1	1.049	0.222	0.53	...	1.017	...	
5	0.2	0.882	2	0.384	0.259	-0.64	1.607	2.390	0.294	
7	0.2	0.892	1	1.067	0.311	1.27	...	0.997	...	
7	0.2	0.892	2	0.430	0.302	-0.17	1.443	2.200	0.321	

5.1. Modes of Kuzmin Disks

Miyamoto (1971) models are characterized by the single parameter n_M . The orbital population becomes more nearly circular with increasing n_M , and ultimately cold in the limit $n_M \rightarrow \infty$. We follow (Hunter 1992) in working with models for which all orbits circulate in the same direction. We use units in which $G = M = R_C = 1$.

The frequencies of the fundamental modes for the self-consistent ($L_0 = 0$) models listed in Table 1 differ substantially from those given earlier by Hunter (1992) and Pichon & Cannon (1997). Those results are incorrect because they omit the boundary integral \mathbf{M}^B . The difference is considerable. Neglecting \mathbf{M}^B gives a pattern speed of $\Omega_p = 0.357$ with $R_{\text{CR}} = 1.717$ and a growth rate of $s = 0.295$ for $n_M = 3$. The true fundamental mode of the $n_M = 3$ model is the compact and rapidly growing central bar shown in Figure 6a, much more compact than that shown in Figure 11 of Pichon & Cannon. The amplitude $P(R)$ of its perturbed density in Figure 6c has a single peak. The secondary mode, shown in the right panels of Figure 6, is slower growing and slower propagating. It is more extensive, has a double-peaked amplitude, and a more spiral structure which is also largely confined within the CR circle. The growth rates and pattern speeds increase with increasing n_M . They become increasingly centrally concentrated as they are largely confined within the CR circle.

The bar charts in Figures 6e and 6f display a standard pattern which is common to all but two of those we show. Angular momentum is lost by the $l < 0$ Fourier components, primarily $l = -1$, and gained by the $l \geq 0$ components. All Fourier components lose $\mathcal{W}_{2,1}$ gravitational energy, much from the $l = -1$ component, while all components gain $\mathcal{K}_{2,1}$ kinetic energy except for $l = -1$. The positive values for the ratio $\mathcal{K}_{2,2}/\mathcal{K}_{2,1}$ for these modes show that the $\mathcal{W}_{2,2}$ and $\mathcal{K}_{2,2}$ terms reinforce this transfer from gravitational to kinetic energy. We show in §6.1 how the forms of the bar charts can be understood in terms of the formulae we derived in §2.3. Every bar chart shows that a few Fourier components are significant for

most of the transfer of angular momentum and energy.

The second block of results in Table 1 are for unidirectional Miyamoto models from which low angular momentum orbits have been removed by applying the cutout function (63) with $L_0 = 0.2$. This removal reduces the active surface density Σ_{act} so that it tends to zero in the center, as shown in the dashed curve in Figure 7c, but does not introduce a sharp barrier. It reduces the active mass M_{act} of the disk by a little more than 10%, but has a much larger effect on the modes, and especially the fundamental mode. The left panels of Figure 7 show the large changes in the fundamental mode of the $n_M = 3$ Miyamoto model caused by the $L_0 = 0.2$ cutout. The amplitude of the fundamental mode is again single peaked, though its peak is moved out to $R \approx 0.4$. This mode rotates so rapidly that no orbits are in CR, and it now extends out to the OLR circle. Its bar chart is totally different from that of Figure 6e, but similar to that of Figure 14e, which is for another fundamental mode of a cutout disk. The $l = -1$ components are small, and the flow of angular momentum and $\mathcal{K}_{2,1}$ is from the $l < 1$ components, primarily $l = 0$, and to the $l \geq 1$ components, primarily $l = 1$.

The cutting-out of low angular momentum orbits and some 10% of the mass reduces the growth rate of the fundamental mode by such a large factor that it is no longer the fastest growing mode. The secondary mode, which is now the fastest growing, is not shown because it is changed much less. It has a similar but smoother spiral shape than that of Figure 6b, and extends just beyond the now-larger CR circle. The two humps of its amplitude $P(R)$ are displaced outwards from those of Figure 6d, and the inner hump, which lies in a region of large mass reduction, is diminished. The outer hump, now at $R \approx 0.9$, lies in a region where the mass reduction is smaller. Hence the reason why the cutout affects the fundamental mode so much more than the secondary mode is that it has a much larger effect on the more central orbits which are the major participants in the fundamental mode than it does on those of the secondary mode. Because the

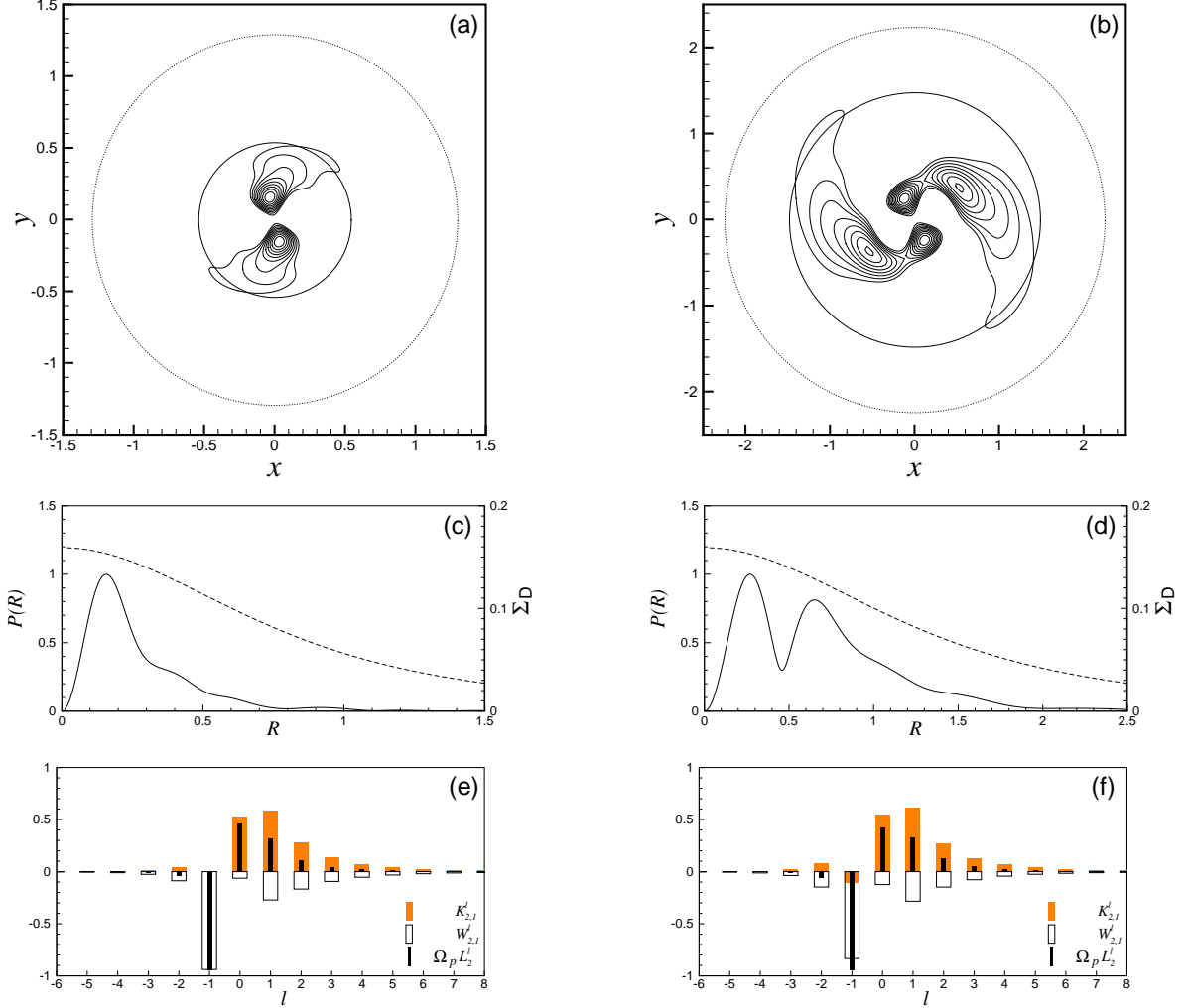


FIG. 6.— The fundamental mode (left panels) and secondary mode (right panels) of the self-consistent $L_0 = 0$, $n_M = 3$, Miyamoto model for Kuzmin’s disk; the first two entries of Table 1. Here and in all subsequent plots of modes, the top panels show positive contours of the perturbed density Σ_1 , in steps of $0.1\Sigma_1$. The solid and dotted circles mark the co-rotation and outer Lindblad resonance circles. The middle panels show the wave amplitude (solid line and left scale) and unperturbed density (dashed line and right scale). The bottom panels show Fourier components of kinetic energy (grey bars), gravitational energy (white bars), and angular momentum (thin bars).

ratio $\mathcal{K}_{2,2}/\mathcal{K}_{2,1} < -1$ for the both modes of the cutout $n_M = 3$ model, both induce a transfer from kinetic to gravitational energy.

The results for higher n_M are similar. The cutout increases the pattern speeds of fundamental modes so much that none have CRs. It decreases the pattern speeds of secondary modes, though not enough for there to be ILRs, which are possible only when $\Omega_p \leq 0.130$. All growth rates are decreased, though the fundamental mode is still, though barely, the faster growing for $L_0 = 0.2$ and $n_M = 7$. As n_M increases and orbits become more circular, the relative amount of angular momentum absorbed by the $l = 1$ component of secondary modes increases.

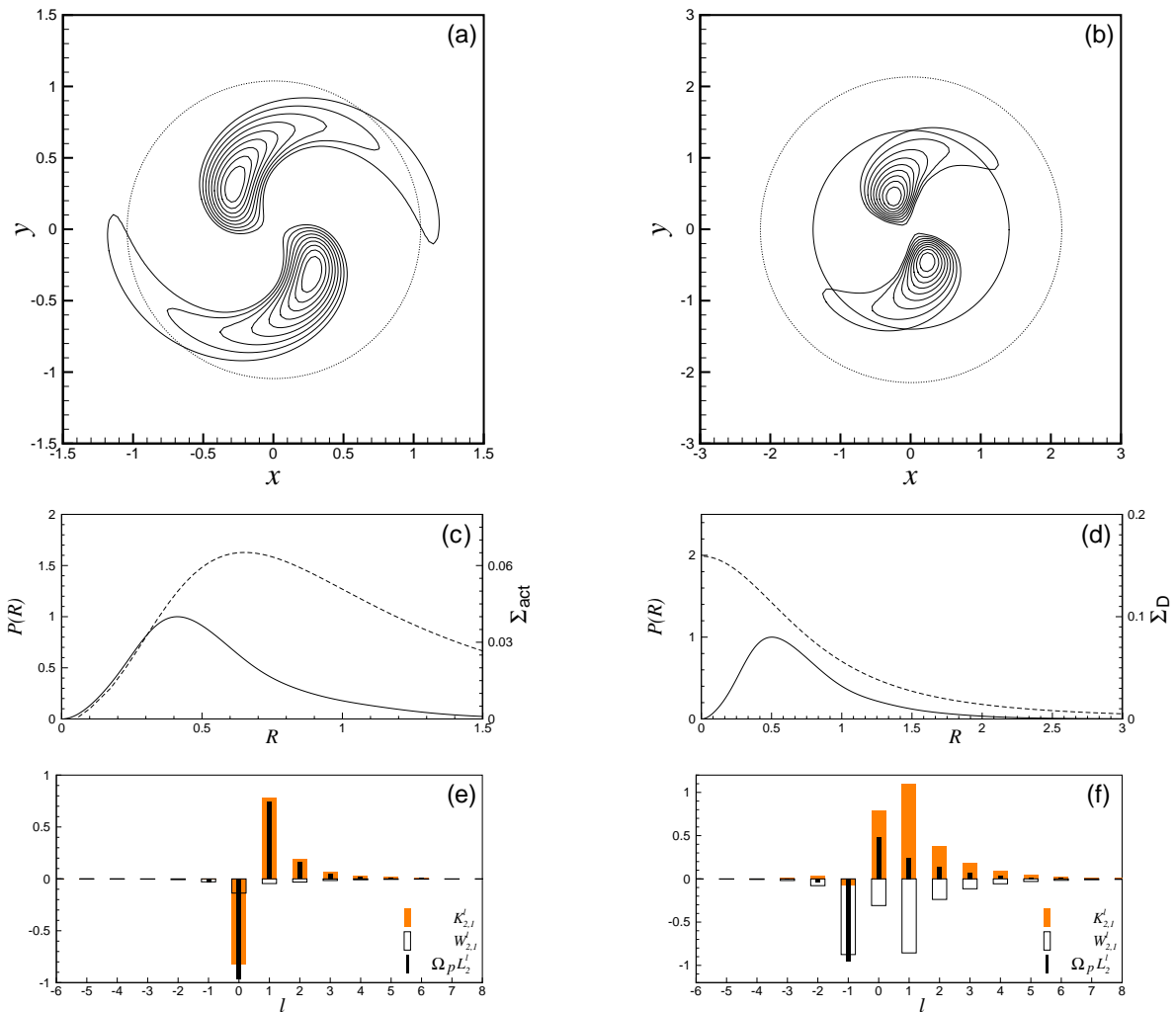
Toomre’s axisymmetric stability parameter Q increases monotonically outwards from its central value of $2\pi/[3.36(1 + n_M/2)^{1/2}]$ for Miyamoto models. Kalnajs (1976b) introduced an alternative set of models, which also depend on an integer parameter m_K which increases as the models cool, and for which Toomre’s Q remains

almost constant. Sellwood & Athanassoula (1986) modified these models with the addition of two extra parameters: an angular momentum J_c and β . They reversed the sense of rotation of a fractional mass M_{retro} of stars in a unidirectional Kalnajs model with angular momenta in the range $(0, J_c)$, following equation (5) of Zang & Hohl (1978). This gives a smoothly tapered DF, and eliminates the discontinuity of the unidirectional model. Our results for some of these models are given in table 2, and displayed in Figures 7 and 8. The fundamental mode of the unidirectional $m_K = 6$ model, listed in Table 2 has not been plotted because it is a compact and rapidly rotating bar, a little larger, but otherwise just like that of the Miyamoto model shown in the left panels of Figure 6. The right panels of Figure 7 show how the compact bar is modified by a tapering with $J_c = 0.25$ which reverses less than 5% of the orbits. Like the cutout, it gives the fundamental mode a smoother, more spiral, and more extensive pattern, and a slower growth rate. A major difference is that the taper diminishes the pattern speed,

TABLE 2. EIGENVALUES FOR $m = 2$ MODES OF ATHANASSOULA & SELLWOOD MODIFIED KALNAJS MODELS FOR KUZMIN'S DISK

m_K	β	J_c	M_{retro}	mode	Full Model			AS ^a		P04 ^b		$l = -1$ only
					Ω_p	s	$\mathcal{K}_{2,2}/\mathcal{K}_{2,1}$	Ω_p	s	Ω_p	s	Ω_p
4	0	0.40	0.084	1	0.335	0.174	1.83	0.168	0.020	0.193
6	0	0	0	1	0.746	0.711	1.42	0.569
6	0	0.25	0.046	1	0.445	0.308	0.52	0.233	0.066	0.22	0.114	0.264
6	0	0.25	0.046	2	0.294	0.109	1.85	0.165	0.058	0.175	0.055	0.207
6	3	0.60	0.154	2	0.158	0.027	-4.00	0.145	0.014	0.14	0.02	0.144
8	4	0.90	0.160	1	0.199	0.064	-1.47	0.173	0.035	0.174

^aAthanassoula & Sellwood (1986)

^bPolyachenko (2004)

 FIG. 7.— The left panels are for the fundamental mode of a cutout $n_M = 3$, $L_0 = 0.2$, unidirectional Miyamoto model. The right panels are for the fundamental mode of a tapered $m_K = 6$, $J_c = 0.25$, Athanassoula & Sellwood model for which some 4.6% of the orbits have been made retrograde.

whereas the cutout increases it. Both the tapering and the cutout cause a large change in the population of low angular momentum orbits which dominate in the central part of the disk where the fundamental mode is concentrated. Whereas the cutout removes many of them, the

tapering merely reverses the rotation of many, and makes the DF isotropic for $|L| \ll J_c$. Figure 7f shows a bar chart which is of the standard pattern, though the tapering has increased the magnitudes of the $l \geq 0$ energy components.

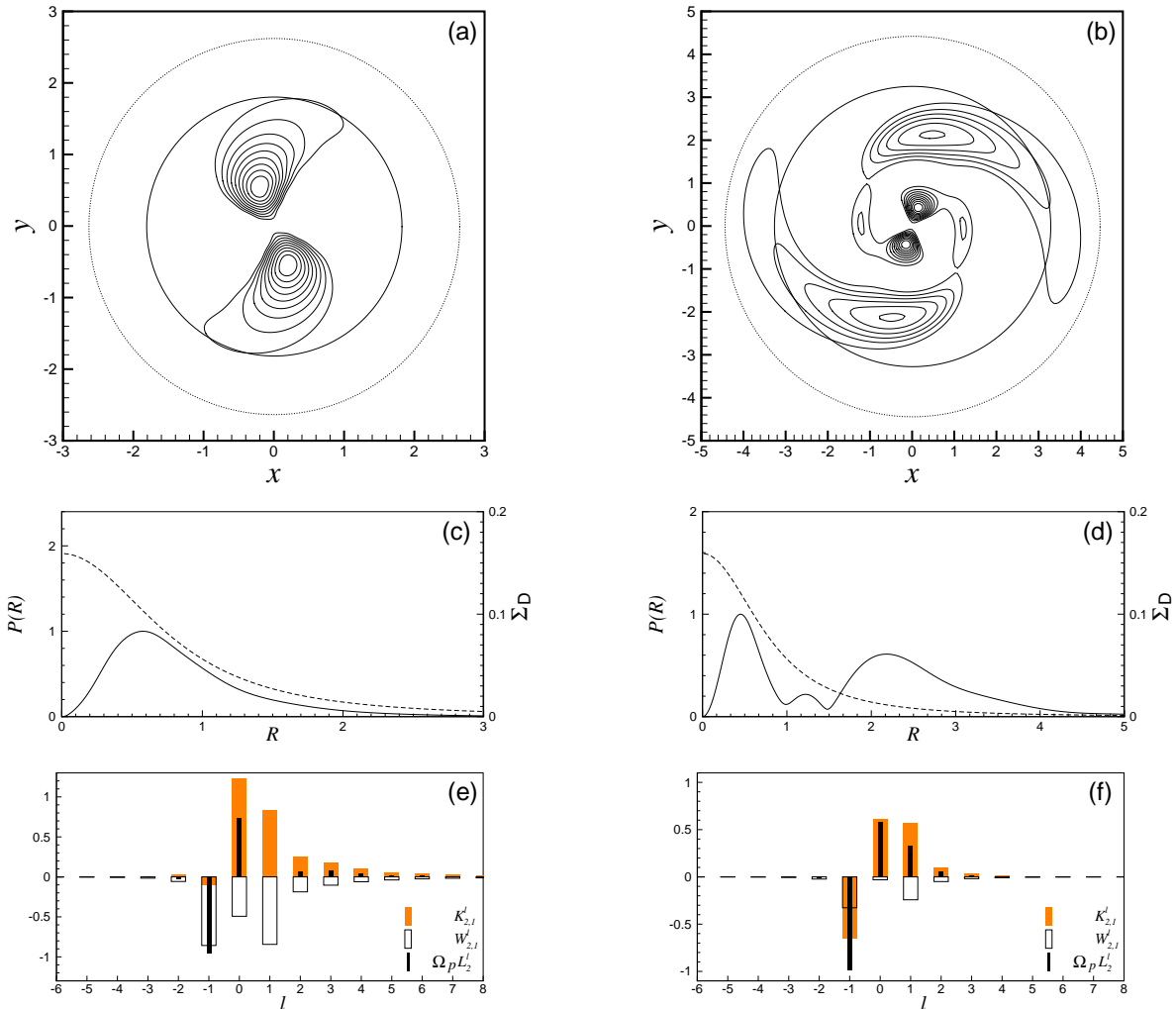


FIG. 8.— The left panels show the fundamental mode of the $m_K = 4$ Athanassoula & Sellwood model, tapered with $J_c = 0.4$ and with 8.4% of its orbits retrograde. The right panels show our computed mode for their $\beta = 3$, $m_K = 6$, $J_c = 0.6$ model with 15.4% retrograde orbits.

We computed the fundamental mode for the tapered $m_K = 4$, $J_c = 0.4$ model because it is one of the few for which Sellwood & Athanassoula plot a mode shape. Our results in the left panels of Figure 8 are similar to, though less spiral than, the fundamental mode of the cooler and more sharply tapered disk in the right panels of Figure 7, though there is a remarkable dearth of angular momentum transferred to its $l = 1$ component. The major difference between their Figure 5b and our Figure 8a is that theirs, which is less spiral, has some central structure which is not present in Figure 8a.

Table 2 compares our results with those of Athanassoula & Sellwood (1986) for four of the 33 models for which they did N -body simulations. Some discrepancies between the matrix theory and the simulations with their finite number of particles and gravity softening are to be expected. Nevertheless, the large discrepancies between our results and theirs, and that of Polyachenko (2004), for the $\beta = 0$ models are worrisome. Our best explanation for it is that we have found these disks to be very sensitive to near-radial orbits, and, as we explain in §4.2 and §4.5, we find eigenvalues to be sensitive to the accu-

racy with which the central regions are handled.

In contrast to these discrepant cases, our results for the two non-zero β models listed in Table 2 agree reasonably well with those of Athanassoula & Sellwood. A positive value of β removes orbits with low energies and angular momentum high relative to $L_c(E)$, and adds to those with higher energies and lower angular momentum. It is easy to show from their Appendix A that

$$f_0(E, 0) = \frac{(m_K - 2\beta E_s^2)}{2\pi^2} \exp[(\beta(1 - E_s^2))], \quad E_s = \frac{R_C E}{GM}. \quad (78)$$

The value of β can not exceed $m_K/2$ because f_0 is then negative at the center of the disk where the scaled energy $E_s = -1$. Many of Athanassoula & Sellwood's models have marginal values $\beta = -m_K/2$. Their f_0 values peak at intermediate values of E_s , and they have double peaked radial velocity profiles. The $(m_K, \beta, J_c) = (6, 3, 0.6)$ model is one of two to which Polyachenko (2004) applied his simplified theory to get a value of the pattern speed Ω_p which agrees with what we get from $l = -1$ terms only. Our plot of the most unstable mode for this case in Figure 8b shows the same concentrated

central structure as in Polyachenko's Figure 6, but his plot has a stronger second hump around $R = 1$ than our weaker one, and lacks the extended outer spiral that we find. The structure of this mode suggests that it is a secondary one, though it is the only one we have found. Its low pattern speed means that it comes closer to having an ILR than any other mode in our survey. Its bar chart in Figure 8f is noteworthy for its large and negative $l = -1$ component of $\mathcal{K}_{2,1}$. This mode is another one for which $\mathcal{K}_{2,2}/\mathcal{K}_{2,1} < -1$, and hence converts kinetic to gravitational energy.

5.2. Modes of Isochrone Disks

Kalnajs (1976b) gives unidirectional models for the isochrone disk. They contain an integer parameter m_K which increases as the models cool, and have fairly uniform values of the Toomre parameter Q . Kalnajs calculated modes for modified versions of these models in which the sense of rotation of some stars is reversed to make them retrograde. Kalnajs's formula for retrograde stars is given in equation (13) of Earn & Sellwood (1995). Combining that with the $x \rightarrow 0$ limit of equation (26) of Kalnajs (1976b) and using GR formula (7.126.1) gives

$$f_0 = \frac{m_K}{6\pi^2 [1 + J_R + |J_\phi|]^{2m_K-2}}, \quad J_\phi < 0, \quad (79)$$

for the DF of retrograde stars in units in which $G = M = R_C = 1$. There are now retrograde stars of all angular momenta, not the limited ranges of the models of §5.1. Integration over phase space gives

$$M_{\text{retro}} = \frac{m_K}{3(m_K - 2)(2m_K - 3)}, \quad (80)$$

for the fractional mass in retrograde stars.

Table 3 gives our results and those of others in units in which $G = M = R_C = 1$ for two modes of these models. The mutual agreement is now gratifyingly close. Both pattern speeds and growth rates increase with increasing m_K , as they do with Miyamoto models with increasing n_M . Pichon & Cannon (1997) found secondary modes for some values of m_K other than those we have listed in our table. Again there are no ILRs. ILRs occur only when $\Omega_p < 0.0593$ in the units used here, for which the ranges of both Ω_R and Ω_ϕ are only a half of what they are in Figure 1.

Figure 9 displays two modes of the isochrone disk with $m_K = 12$. The wave patterns match those of Earn & Sellwood's Figure 1. Spirality increases with m_K . The secondary mode is more extended than the fundamental, and the amplitude of its spiral arm is two-peaked, versus the single peak of the fundamental mode. Both bar charts show that the $l = 1$ component absorbs much more angular momentum and kinetic energy than the $l = 0$. This is different from Figure 6, but is in line with the trend we noted with Miyamoto models with increasing n_M , though note that $m_K = 12$ corresponds to a much larger n_M value than the $n_M = 3$ of Figure 6. The secondary mode of the warmest $m_K = 6$ model is the only one for which kinetic is converted to gravitational energy.

We studied some other models for the isochrone potential, and found, as did Pichon & Cannon (1997), that their modes are qualitatively similar to those for Kuzmin's disk. Only their scales differ because the isochrone disk is the more spread out.

5.3. Modes of the Exponential Disk

Our exponential disk models are the most varied. After normalizing with units in which $G = v_0 = R_C = 1$, we are still left with three parameters; N which measures the tendency of the orbits to circularity (cf Figure 5), R_D which measures the length scale of the exponential disk relative to the core radius of the potential, and the density scale Σ_s . A cutout introduces a further parameter L_0 . The central density of the disk is $\Sigma_s e^{-\lambda}$ and its total mass $M_D = 2\pi\Sigma_s R_D(R_C + R_D)e^{-\lambda}$. As Figure 5a shows, disks become increasingly centrifugally supported with increasing N and hence this parameter is similar to the parameters n_M and m_K which we varied for previous models. Here we restrict our exponential disk models to the single case of $N = 6$ to allow us to study the consequences of varying the other parameters. As Figure 5b shows, $N = 6$ models have Toomre's Q parameter close to unity over a substantial central part of the disk, whose size increases with R_D when $R_D \geq 1$.

Table 4 lists the fundamental and secondary modes for six different $N = 6$ models. It lacks values of the ratio $\mathcal{K}_{2,2}/\mathcal{K}_{2,1}$ because we were unable to compute accurate values of $\mathcal{K}_{2,2} = -\mathcal{W}_{2,2}$ with our chosen basis functions, for the reasons discussed in §4.1. ILRs occur in the cored logarithmic potential only for $\Omega_p < 0.106$, which is much smaller than any of the pattern speeds. Figure 10 shows the two modes for the first $R_D = 1$, $\Sigma_s R_D = 0.42$, model. The fundamental mode is a rapidly rotating bar confined within the CR circle, and similar in all respects to that of the Kuzmin disk in Figure 6a. The secondary mode has a slightly lower pattern speed and growth rate, and has a spiral form. Its amplitude has the usual two peaks within the CR circle, and its pattern extends a little beyond the CR circle but lies within the OLR circle. Its bar chart is remarkable for its small $l = 0$ components.

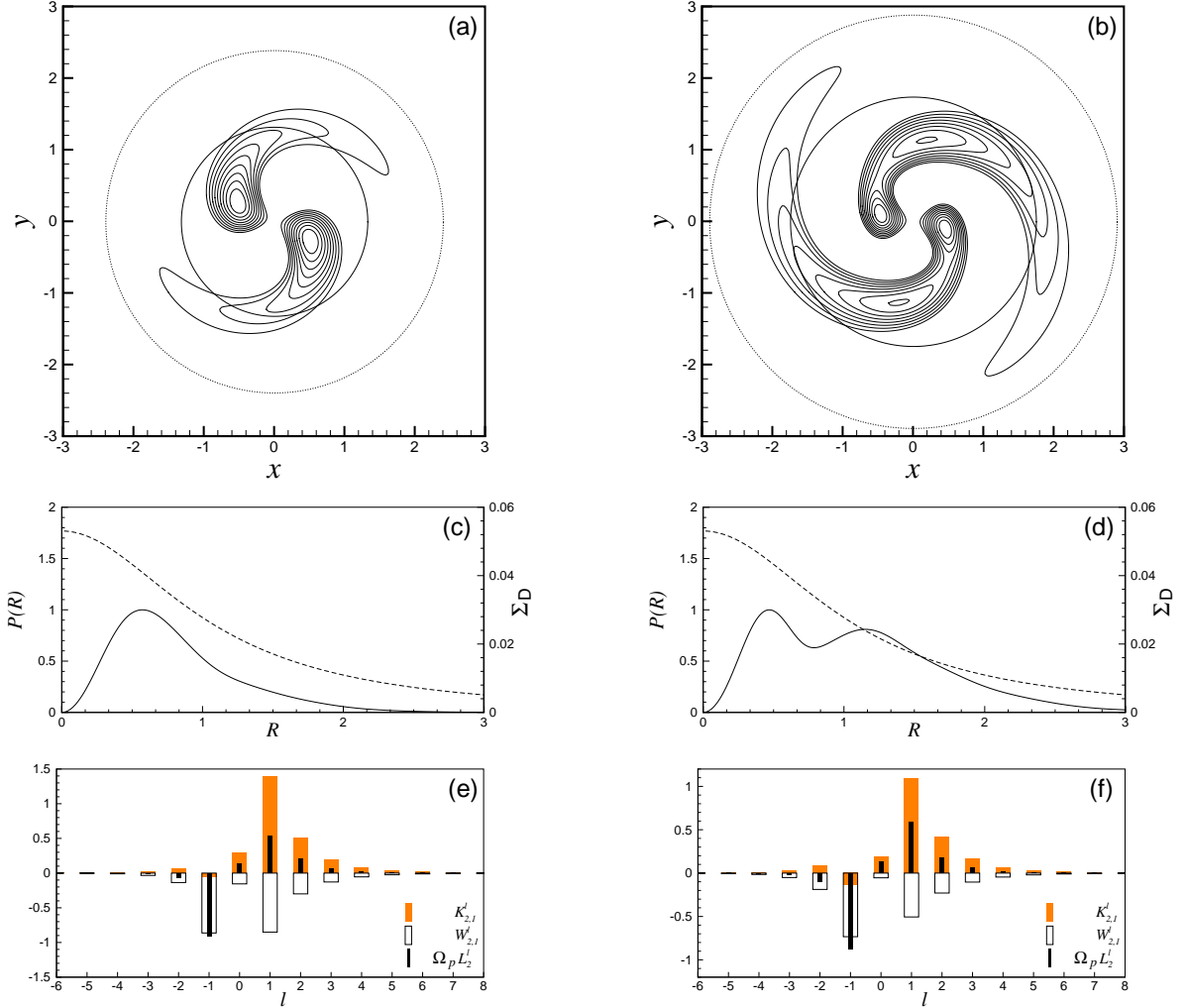
The first four models of Table 4 are chosen to study the effect of varying R_D . The parameter $\Sigma_s R_D$ has to be changed too because it is necessary to remain within the physically allowed region of Figure 2. Its values are near marginal in that they are approximately 90% of their allowed maximum. Despite the decrease of $\Sigma_s R_D$, the total disk mass grows as its scale length R_D increases, though, as Figure 3 shows, the halo/bulge grows in importance as R_D decreases, and the disk becomes progressively less maximal. The structure of the fundamental bar mode does not change along this sequence; it remains a compact and rapidly rotating central bar. Figure 11b for $R_D = 1.6$ shows that the amplitude of the secondary mode has developed a third hump. This development occurs around $R_D \approx 1.25$, and seems to be related to the anomalously low growth rate at $R_D = 1.2$ (See Table 4). The biggest difference between the bar chart Figure 11c for the larger $R_D = 1.6$ disk and that of Figure 10f for $R_D = 1$ is the greatly increased significance of the $l = 0$ component.

Figures 12 and 13 illustrate how decreasing Σ_s and hence the mass of the disk, whilst keeping its length scale R_D fixed, stabilizes the disk. The transition of the fundamental mode from stability to instability appears to take place through a pitchfork bifurcation. That of the secondary mode appears to take place through a tangent bifurcation. The order in which the two modes are stabilized is different for the two different values of R_D .

TABLE 3. EIGENVALUES OF KALNAJS MODELS FOR THE ISOCCHRONE DISK.

m_K	M_{retro}	mode	Full Model			K78 ^a		PC97 ^b		$l = -1$ only
			Ω_p	s	$\mathcal{K}_{2,2}/\mathcal{K}_{2,1}$	Ω_p	s	Ω_p	s	Ω_p
6	0.056	1	0.169	0.080	-0.11	0.170	0.075	0.170	0.075	0.094
6	0.056	2	0.121	0.035	-1.58	0.079
9	0.029	1	0.235	0.149	-0.05	0.235	0.145	0.235	0.145	0.127
9	0.029	2	0.183	0.089	-0.92	0.109
12	0.019	1	0.292	0.217	0.07	0.295	0.210	0.295	0.210	0.150
12	0.019	2	0.234	0.148	-0.60	0.230	0.145	0.133

^aKalnajs (1978).

^bPichon & Cannon (1997).

 FIG. 9.— Fundamental mode (left panels) and secondary mode (right panels) of the isochrone disk with $m_K = 12$.

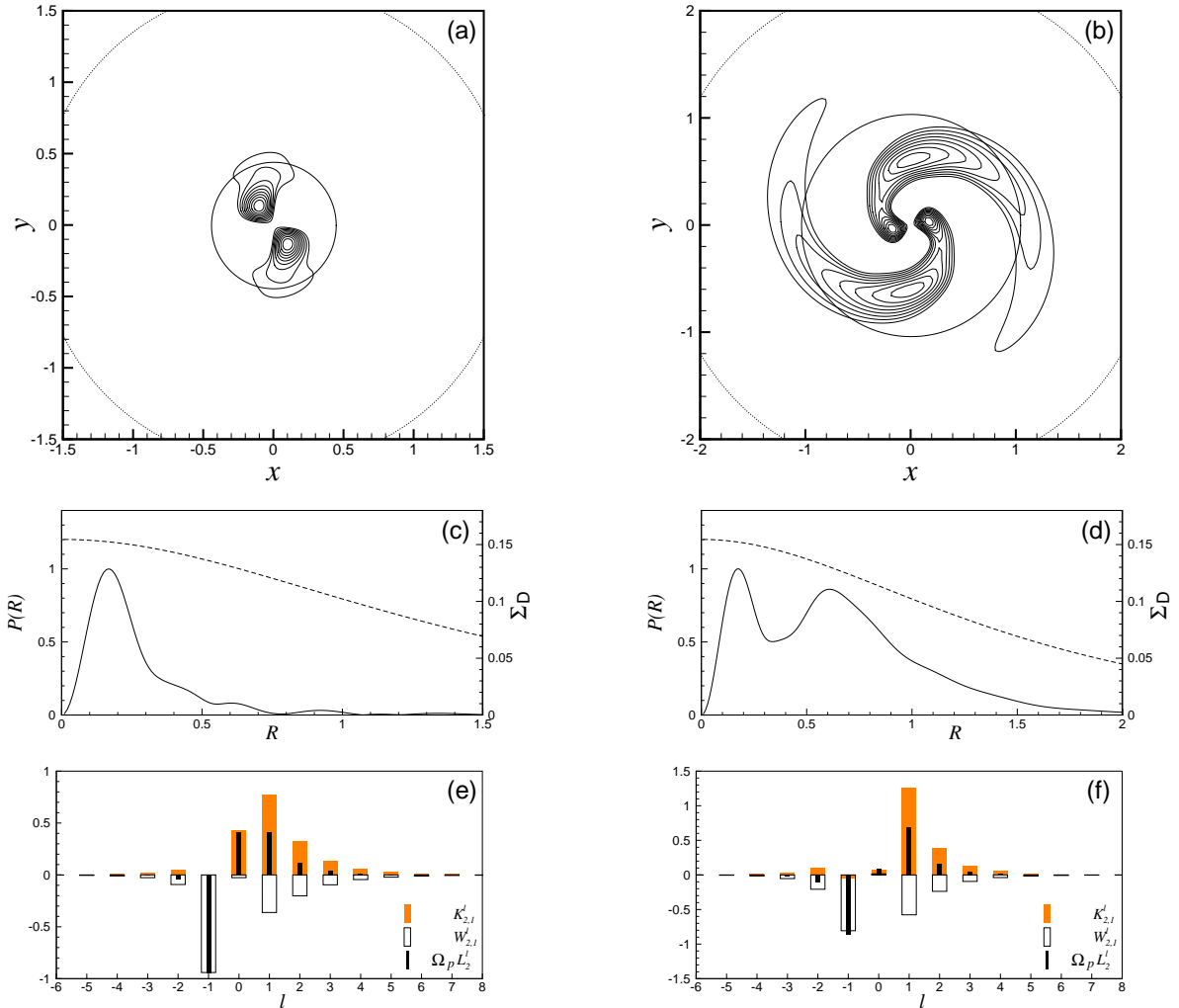
When $\Sigma_s R_D$ is decreased at a fixed R_D , then the part of the rotational velocity due to the halo/bulge components increase from those shown in Figure 3 which are drawn for values of $\Sigma_s R_D$ which are 90% of the allowed maximum. The stabilization shown in figures 12 and 13 is therefore similar to that which is achieved by sufficiently massive halos (Kalnajs 1972, Ostriker & Peebles 1973,

Hohl 1975).

The stabilization of both modes in the neighborhood of $\Sigma_s R_D \approx 0.3$ for both $R_D = 1$ and $R_D = 1.6$ suggests that the stability boundary approaches the boundary of the physically feasible region plotted in Figure 2 as R_D increases, i.e. as λ decreases. It raises the possibility that the two boundaries intersect before the $\lambda \rightarrow 0$ limit

TABLE 4. EIGENVALUES FOR $m = 2$ MODES OF EXPONENTIAL DISKS WITH $N = 6$.

mode	R_D	$\Sigma_s R_D$	L_0	M_{act}	Full Model				$l = -1$ only
					Ω_p	s	R_{CR}	R_{OLR}	Ω_p
1	1	0.42	0	1.000	0.914	1.151	0.444	1.688	0.698
2	1	0.42	0	1.000	0.693	0.324	1.040	2.334	0.364
1	1.2	0.38	0	1.000	0.840	0.935	0.646	1.871	0.591
2	1.2	0.38	0	1.000	0.607	0.059	1.309	2.701	0.330
1	1.4	0.36	0	1.000	0.805	0.794	0.737	1.967	0.540
2	1.4	0.36	0	1.000	0.467	0.179	1.893	3.572	0.294
1	1.6	0.34	0	1.000	0.768	0.642	0.834	2.077	0.488
2	1.6	0.34	0	1.000	0.443	0.119	2.024	3.775	0.277
1	1	0.42	0.1	0.967	1.170	0.259	...	1.212	...
2	1	0.42	0.1	0.967	0.537	0.288	1.571	3.082	0.331
1	1	0.42	0.3	0.913	1.044	0.228	...	1.423	...
2	1	0.42	0.3	0.913	0.439	0.274	2.047	3.811	0.302

FIG. 10.— Modes of the exponential disk for $N = 6$, $R_D = 1$, and $\Sigma_s R_D = 0.42$. The left panels are for the fundamental mode, and the right panels are for the secondary mode.

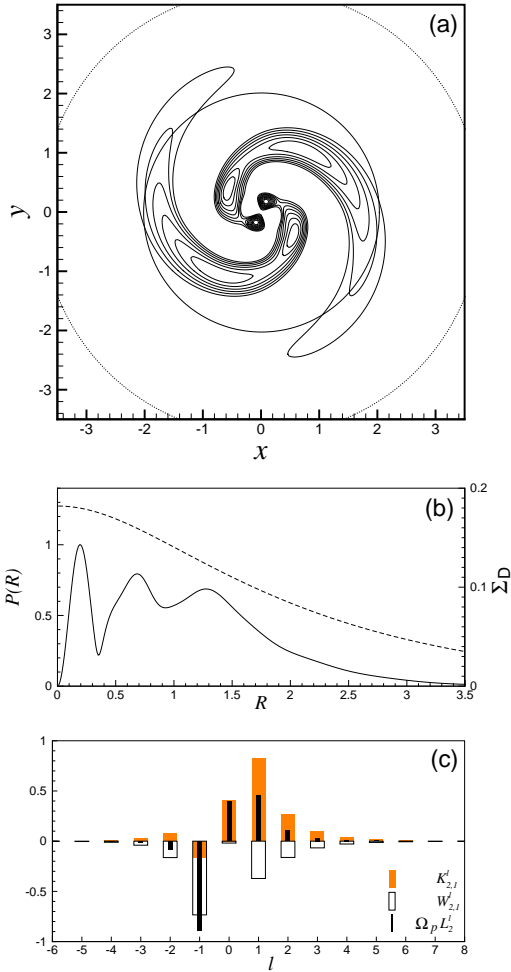


FIG. 11.— The secondary mode of an $N = 6$ exponential disk of larger extent with $R_D = 1.6$ and $\Sigma_s R_D = 0.34$.

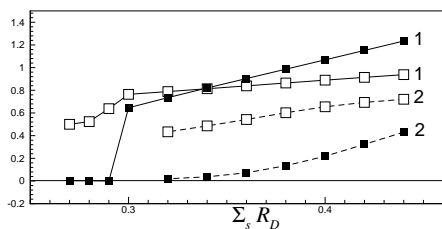


FIG. 12.— The variation of the pattern speed Ω_p (open squares) and growth rate s (filled squares) of the $N = 6$, $R_D = 1$ exponential disk as the mass of the disk is varied. Data for the fundamental modes (1) and secondary modes (2) are connected by solid and dashed lines, respectively. The secondary modes are double peaked.

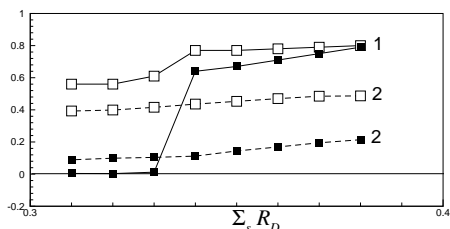


FIG. 13.— Same as Figure 12 but for $N = 6$, $R_D = 1.6$. The secondary modes now have triple peaks.

of an exponential disk in a singular logarithmic potential, for which $\Sigma_s R_D = 0.304$ is reached. Our current computer algorithms are not capable of approaching that limit, but they do show the $R_D = 2$ disk to be quite stable. This suggests that the classical exponential disk ($\lambda = 0$) with a completely flat rotation curve ($R_C = 0$) may be stable against bisymmetric excitations. This disk is much less than maximal, and requires a substantial central bulge/halo to maintain its equilibrium.

The final Figure 14 and the last two models of Table 4 show the effect of cutting out low angular momentum orbits via the cutout function (63). There is a major change between $L_0 = 0$ and $L_0 = 0.1$. Comparison with Figure 10 shows that the fundamental mode is changed much more than the secondary one, as we found with the Kuzmin disk. Its growth rate is diminished substantially, and its pattern speed is increased so much that there is no longer a CR circle. It is more spiral and extensive as the peak of its amplitude has moved outwards from the region in which the density has been diminished substantially. Its bar chart has undergone a large change and now resembles that of Figure 7e; the $l = -1$ components are insignificant and the flow of both angular momentum and $K_{2,1}$ is primarily from $l = 0$ to $l = 1$. The growth rate and pattern speed of the more extensive secondary mode is changed much less by the cutout. The decrease in the inner density of the disk leads to the near total disappearance of the inner hump of its amplitude. The $l = 0$ components are again significant in the bar chart of Figure 14f, unlike the $R_D = 1$ case of Figure 10f, but like that for the $R_D = 1.6$ case of Figure 11c. The modes for $L_0 = 0.3$ are similar to those for $L_0 = 0.1$. The singular behavior of e^{-L^2/L_0^2} makes the study of small values of L_0 and the approach to the limit $L_0 \rightarrow 0$ computationally difficult.

We can not compare our results directly with those of Sellwood (1989) which are for uncored exponential disks in the cored logarithmic potential (50). Not only are the disks different, but his are for the larger range $2 \leq R_D/R_C \leq 8.33$ of disk radii than ours. His $m = 2$ modes have pattern speeds that are also too fast for ILRs, but the spiral mode for $R_D/R_C = 5$ shown in the left of his Figure 3 extends out to the OLR circle, and so is more extensive than any of ours for exponential disks without cutouts. As noted in §3.4, Sellwood's value of 0.6 for the critical parameter $v_0(R_D/GM_D)^{1/2}$, which corresponds to $[e^\lambda/2\pi\Sigma_s R_D(1+\lambda)]^{1/2}$ in our scalings, is smaller than any of ours. That critical parameter is 0.86 when stability is achieved for $\Sigma_s R_D = 0.29$ in Figure 12 for example. That value is still significantly less than the 1.1 which Efstathiou, Lake & Negroponce (1982) found to be necessary for their N -body experiments, but that larger value may well be necessary for nonlinear stability.

6. DISCUSSION

We analyze and explain the properties of the bar charts in §6.1, and discuss the implications of our findings for Polyachenko's (2004) simplified theory in §6.2.

6.1. Transfer of Angular Momentum and Energy

The rate of change of the perturbed angular momentum (A6) contains a factor $s/|l\Omega_R + m\Omega_\phi - \omega|^2$, which tends to $\pi [m(\Omega_\phi - \Omega_p) + l\Omega_R]$ as $s \rightarrow 0$. As Lynden-Bell

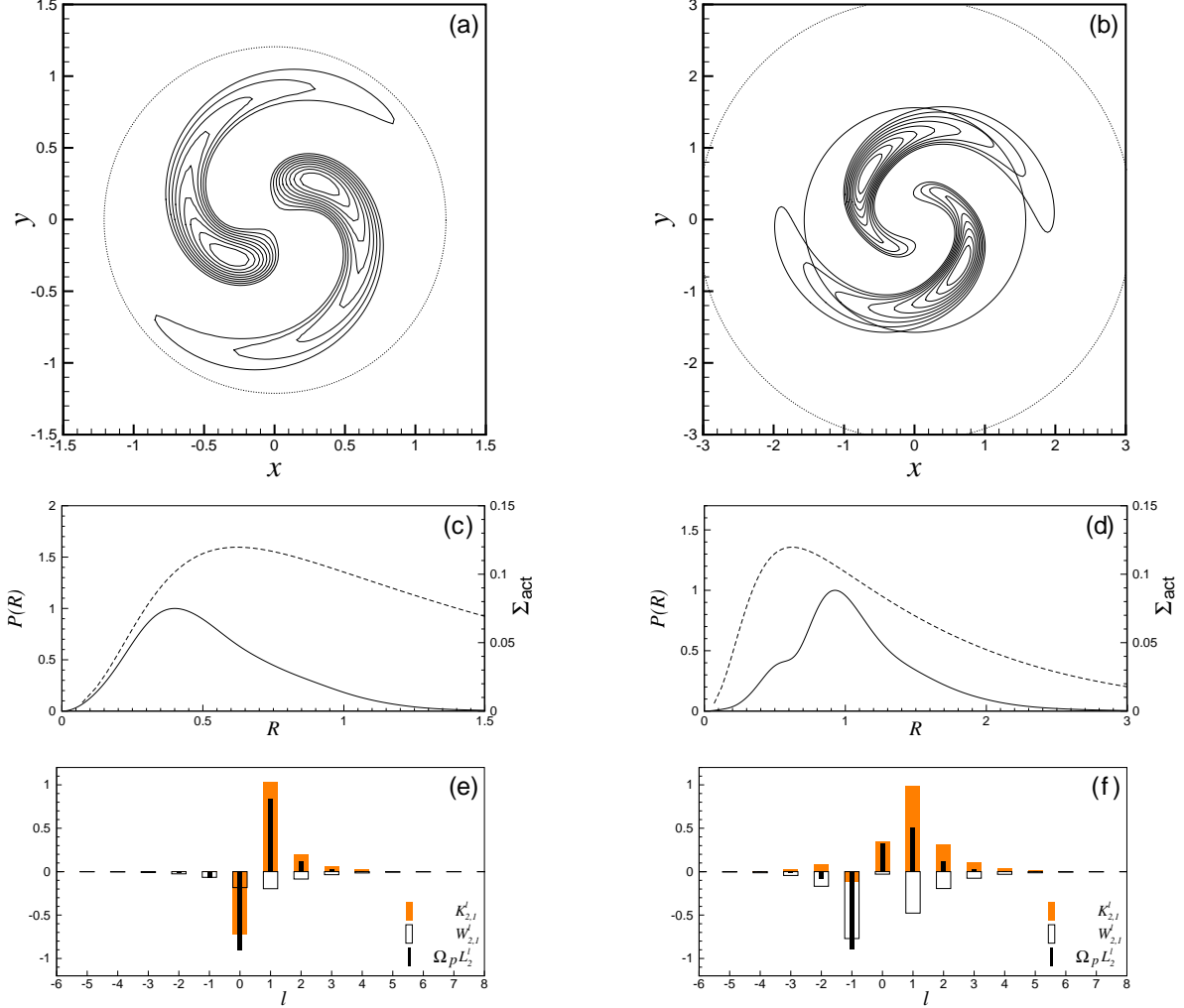


FIG. 14.— Modes of the $N = 6$, $R_D = 1$, and $\Sigma_s R_D = 0.42$ exponential disk with an $L_0 = 0.1$ cutout. The active surface density is shown by the dashed lines in the central panels. The left panels show the fundamental mode and the right panels the secondary mode.

& Kalnajs (1972) note, this implies that a neutrally stable wave emits and absorbs angular momentum only at resonances. For the unstable modes we discuss, the factor $s/|l\Omega_R + m\Omega_\phi - \omega|^2$ peaks at resonances, sharply so when s is small. This peaking implies that emission and absorption occurs mainly near resonances. Figure 1 shows that, for given pattern speed $\Omega_p > 0$, the orbits associated with $l \geq 0$ resonances lie at successively smaller values of the orbital frequencies Ω_R and Ω_ϕ , and hence successively further out in the disk. That is the reason for interpreting the flows of angular momentum, and also kinetic energy, which are proportional to the quantities shown in the bar charts, as outward flows.

It is evident from equations (35), (37), and (38) that the partial derivatives $\partial f_0/\partial J_R$ and $\partial f_0/\partial J_\phi$ play a major role in determining the signs of the Fourier components shown in the bar charts. All the other terms in L_2^l are either magnitudes or constants. Lynden-Bell & Kalnajs argued that both derivatives are negative for a physically reasonable DF. If this is so, then equation (37) shows that $L_2^l > 0$ for $l \geq 0$. The compensating negative values of L_2^l , necessary because there is no net change of angular momentum, can and must occur for

$l < 0$. The fact that L_2^{-1} is negative, as we find, can be accounted for by $|\partial f_0/\partial J_R|$ being much larger than $|\partial f_0/\partial J_\phi|$. The prediction matches the standard pattern we find in §5. The assumptions that $\partial f_0/\partial J_R < 0$ and $|\partial f_0/\partial J_R| \gg |\partial f_0/\partial J_\phi|$ are generally valid. Figure 6 of Kalnajs (1976b) gives examples; the contours of the two unidirectional DFs shown there decrease much more rapidly with increasing J_R than with J_ϕ . However the modified $\beta = m_K/2$ models of §5.1 are exceptional because they have regions in which $\partial f_0(E, L)/\partial E$, and hence $\partial f_0(J_R, J_\phi)/\partial J_R$, are positive.

Though positive values of $\partial f_0/\partial J_R$ are unusual, positive values of $\partial f_0/\partial J_\phi$ are not. They are unavoidable with disks which are totally, or mostly, unidirectional. If $f_0^P(J_R, 0) = 0$, as it is for the unidirectional models of Zang (1976) and Evans & Read (1998a) and our cutout disks, then $\partial f_0/\partial J_\phi$ must be positive for some positive values of J_ϕ because otherwise $f_0(J_R, J_\phi)$ could never become positive for $J_\phi > 0$. Similarly $\partial f_0/\partial J_\phi$ must be positive for some $J_\phi > -J_c$ for the tapered models of Table 2. Furthermore the explicit formula (79) shows that $\partial f_0/\partial J_\phi > 0$ for $J_\phi < 0$ for the isochrone models of §5.2. Although no positive values of $\partial f_0/\partial J_\phi$ are visible

in Figure 6 of Kalnajs (1976b), these are disks for which the boundary integral

$$-m^2\pi^2 \int dJ_R \left[\frac{f_0^P(J_R, 0) |\tilde{V}_l|^2}{|\Omega_R + m\Omega_\phi - \omega|^2} \right]_{J_\phi=0}, \quad (81)$$

must then be included in the expression for L_2^l . It is negative for every l , as are the contributions to the integral (37) from positive values of $\partial f_0/\partial J_\phi$. Unidirectional disks for which $f_0^P(J_R, 0) > 0$ can be regarded as $J_c \rightarrow 0$ limits of tapered disks; the boundary integral (81) then accounts for the effect of the large positive values of $\partial f_0/\partial J_\phi$ which occur in the taper.

Despite the occurrence of regions of positive values of $\partial f_0/\partial J_\phi$, they are generally either too small, or confined to too limited regions, to modify the standard bar chart pattern. However, cutout disks have central regions in which $\partial f_0/\partial J_\phi$ is large and positive. That is the reason for the negative values of L_2^0 in the bar charts of Figures 7e and 14e for fundamental modes of cutout disks. The bar charts for the secondary modes of these cutout disks have the standard form, as is seen in Figure 14f. This is because $\partial f_0/\partial J_\phi < 0$ for the more distant orbits which are the more important for the secondary mode.

Integral (38) for $K_{2,1}^l$ differs from integral (37) for L_2^l by a factor $(\Omega_\phi + l\Omega_R/2)$. This is positive for $l \geq -1$ for all direct orbits, but negative for $l \leq -2$ (See Figure 1), and is the reason why the signs of $K_{2,1}^l$ match those of L_2^l for $l \geq -1$, but are their opposites for $l \leq -2$. This pattern holds even for the exceptional cases, with the result that $K_{2,1}^l$ is positive for all l , except for $l = -1$ in standard bar charts and $l = 0$ in our exceptional ones.

Integral (35) for $W_{2,1}^l$ differs from that for L_2^l by a factor $(\Omega_p - \Omega_\phi - l\Omega_R/2)$. This factor is positive for all orbits for $l = 0$ modes when the pattern speed $\Omega_p > 1$, which is why $W_{2,1}^0$ is negative like L_2^0 for the exceptional fundamental modes. $W_{2,1}^0$ and L_2^0 otherwise have opposite signs for other modes with slower pattern speeds and $L_2^0 > 0$, and which are dominated by orbits within CR. In fact $W_{2,1}^l$ is negative for all l in all bar charts. This is explained by noting that $(\Omega_p - \Omega_\phi - l\Omega_R/2)$ is negative for modes which lie principally within OLR for $l \geq 1$, and positive for $l \leq -1$, so that the signs of $W_{2,1}^l$ are respectively the opposite and the same as those of L_2^l .

A striking feature of the bar charts is the rapidity with which the quantities displayed there decrease with increasing $|l|$. There are two reasons for this. One is the increase in the denominators of their integrands in the regions where most orbits lie. The $l = -1$ terms are generally important, even though there is no ILR, because the denominator term $2(\Omega_\phi - \Omega_p) - \Omega_R$ is never large for any orbit. Another reason is the decay of the Fourier coefficients \tilde{V}_l with increasing $|l|$.

6.2. Abnormal Orbits and Polyachenko's Theory

Tables 1 through 4 show consistently that eigenvalues estimated using Polyachenko's simplified theory are lower than those calculated from the full matrix theory. Pattern speeds Ω_p well exceed the narrow range of Ω_i values which the cored potentials considered here allow, and so his basic assumption of small $|\Omega_p - \Omega_i|$ is then not valid. Our bar charts show clearly that a few

Fourier components other than $l = -1$ are always significant. The orbits which participate in the unstable modes that we find are predominantly abnormal in the sense defined by Lynden-Bell (1979) because all sufficiently central, as well as more radial, orbits are abnormal. In fact even circular orbits are normal only for $R/R_C > 2.44$ for Kuzmin's disk, $R/R_C > 3.73$ for the isochrone, and $R/R_C > 25.3$ for the cored logarithmic potential (See Figure 4). Our modes lie primarily within these limits.

A quite different situation arises with the scale-free potentials $V_0(R) = \text{sgn}(\alpha)R^\alpha$ for $\alpha \neq 0$, and $V_0(R) = \ln R$ for $\alpha = 0$, studied by Evans & Read (1998a,b). Even central orbits can then be normal because the normal/abnormal classification then depends solely on the ratio $y = L/L_c(E)$, and is independent of energy. Lynden-Bell's criterion (44) is satisfied, and an orbit abnormal, if

$$- \left[f(y) + \frac{\pi y}{2} \right]^2 f''(y) - \left[\frac{2-\alpha}{2+\alpha} \right] \left[f'(y) + \frac{\pi}{2} \right]^2 [f(y) - yf'(y)] > 0, \quad (82)$$

where the function $f(y) = \pi J_R/L_c(E)$ and depends also on α . Its derivative $f'(y) = -\pi\Omega_\phi/\Omega_R = \frac{1}{2}|g(\alpha, y)|$, where $g(\alpha, y)$ is the function defined and analyzed in Touma & Tremaine (1997). The criterion (82) gives $y < 0.723$ for the scalefree logarithmic potential, so that all the more circular orbits with large $L/L_c(E)$ are normal. For $\alpha = -0.25$ and a falling rotation curve, there is a wide range of normal orbits, and only orbits with $y < 0.496$ are abnormal. For $\alpha = 0.25$ and a rising rotation curve, only nearly circular orbits are normal, and all those with $y < 0.973$ are abnormal. All orbits are abnormal for $\alpha > 0.275$. Interestingly Evans & Read, who looked specifically at the cases of $\alpha = \pm 0.25$, found that unstable modes grow more vigorously for the rising rotation curve case of $\alpha = 0.25$ with many abnormal orbits. ILRs occur with their modes because the range of Ω_i is unbounded for scale-free potentials.

7. SUMMARY

This paper develops the theory of modes in thin stellar disks. It then implements that theory for a selection of disks. The theory basically is that pioneered by Kalnajs (1971,1977). Our development of its Eulerian form to second order is new. The expressions for angular momentum and total energy were given earlier by Kalnajs (1971) and Lynden-Bell & Kalnajs (1972), but the expressions for the two separate components are new. The boundary integral terms which must be included in the method are also new. These integrals are avoided when a Lagrangian form of the theory is used. The Lagrangian form leads to more complicated computations, which is why prior computational work, except for that of Vandervoort (1999), has all been done for using the Eulerian form. We show in Appendix B how the passage from the Lagrangian to the Eulerian form allows us to interpret the boundary integrals as boundary fluxes. This analysis does not apply to the quite different version of Lagrangian theory which Vandervoort uses.

Our applications of the theory are to $m = 2$ modes in potentials with smooth cores. In all but one case (see Table 2), our search has found two modes, a centrally

concentrated fundamental mode with a single peak in amplitude, and a more extensive and more spiral secondary mode with at least two peaks. There may be others. We find that the shape, pattern speed, and growth rate of the fundamental mode are especially sensitive to the relatively small proportion of orbits which provide the density in central regions because they have low angular momentum. The growth rate of the fundamental mode is reduced substantially, and its shape becomes more extensive and spiral, if those orbits are either removed or reversed. Removing them increases the pattern speed, while reversing them decreases it. Removing them also makes the more extensive and more spiral secondary mode the faster growing in all but one of the cases in Tables 1 and 4. This sensitivity to orbits, many of which are near radial, might suggest a connection with the phenomenon of *radial orbit instability*. However that phenomenon, reviewed recently in Merritt (1999), occurs in hot anisotropic spherical stellar systems in which radial orbits are sufficiently predominant. The sensitivity we find here arises even with cool stellar systems with few near radial orbits.

With two exceptions, modes are largely confined within the CR circle, but are too fast for there to be any or-

bits in ILR. The lack on an ILR means that modes can propagate into, and be reflected from, the center of the disk, even in cases in which our densities drop to zero there. The modes are unstable, sometimes rapidly so, as swing-amplifier theory (Toomre 1981) predicts. We have achieved stability only by decreasing the active mass of the disk. In the exceptional cases, the modes lie within the OLR circle, and the pattern speeds are then too fast for any orbits to be in CR. All the unstable modes transfer angular momentum and kinetic energy outwards, and most release gravitational energy and convert it to kinetic energy. This flow of angular momentum and energy is derived from the second order extension of a linear theory, and so can describe only the early stages of the growth of an instability, and not its later fully nonlinear development. Only a few Fourier components account for almost all of the angular momentum and energy. Polyachenko's (2004) theory, which is equivalent to ignoring all but one term of our Fourier development, seems to be an oversimplification.

This work has been supported in part by the National Science Foundation through grant DMS-0104751.

REFERENCES

- Aoki, S., & Iye, M. 1978, PASJ, 30, 519
 Athanassoula, E., & Sellwood, J. A. 1986, MNRAS, 221, 213
 Binney, J., & Tremaine, S. 1987, Galactic Dynamics (Princeton: Princeton Univ. Press)
 Boccaletti, D., & Pucacco, G. 1996, Theory of Orbits (New York: Springer)
 Brogan, W. L. 1990, Modern Control Theory (New York: Prentice Hall)
 Clutton-Brock, M. 1972, Ap&SS, 16, 101
 Davis, P. J., & Rabinowitz, P. 1984, Methods of Numerical Integration, 2nd ed. (Orlando: Academic Press)
 de Zeeuw, P. T., & Hunter, C. 1990, ApJ, 356, 365
 Earn, D. J. D., & Sellwood, J. A. 1995, ApJ, 451, 533
 Efstathiou, G., Lake, G., & Negroponte, J. 1982, MNRAS, 199, 1069
 Evans, N. W., & de Zeeuw, P. T. 1992, MNRAS, 257, 152
 Evans, N. W., & Collett, J. L. 1993, MNRAS, 264, 353
 Evans, N. W., & Read, J. C. A. 1998a, MNRAS, 300, 83
 Evans, N. W., & Read, J. C. A. 1998b, MNRAS, 300, 106
 Freeman, K. C. 1970, ApJ, 160, 811
 Gerhard, O. E. 1991, MNRAS, 250, 812
 Giovanelli, R., & Haynes, M.P. 2002, ApJ, 571, L107
 Gradshteyn, I. S., & Ryzhik, I. M., 1980, Table of Integrals, Series and Products (New York: Academic Press) (GR)
 Hohl, F. 1971, ApJ, 168, 343
 Hohl, F. 1975, in IAU Symp. 69, Dynamics of Stellar Systems, ed. A. Hayli (Dordrecht: Reidel) 349
 Hunter, C. 1992, in Astrophysical Disks, ed S. F. Dermott, J. H. Hunter Jr., & R. E. Wilson (New York: Annals NY Acad. Sci. 675), 22
 Hunter, C. 2002, in ASP Conf. Ser. 275, Disks of Galaxies: Kinematics, Dynamics and Perturbations, ed. E. Athanassoula, A. Bosma, & R. Mujica (San Francisco: ASP), 293
 Kalnajs, A. J. 1971, ApJ, 166, 275
 Kalnajs, A. J. 1972, ApJ, 175, 63
 Kalnajs, A. J. 1976a, ApJ, 205, 745
 Kalnajs, A. J. 1976b, ApJ, 205, 751
 Kalnajs, A. J. 1977, ApJ, 212, 637
 Kalnajs, A. J. 1978, in IAU Symp. 77, Structure and Properties of Nearby Galaxies, ed. E. M. Berhuijsen & R. Wielebinski (Dordrecht: Reidel) 113
 Kormendy, J. 1977, ApJ, 217, 406
 Kuzmin, G. G. 1956, AZh, 33, 27
 Landau, L. D. 1946, J. Phys. USSR, 10, 25
 Lin, C. C., & Shu, F. H. 1964, ApJ, 140, 646
 Lindblad, B. 1959, in Handbuch der Physik, 53, ed S. Flügge (Berlin: Springer), 21
 Lynden-Bell, D. 1979, MNRAS, 187, 101
 Lynden-Bell, D., & Kalnajs, A. J. 1972, MNRAS, 157, 1
 Merritt, D. 1999, PASP, 111, 129
 Mestel, L. 1963, MNRAS, 126, 553
 Miller, R. H., Prendergast, K. H., & Quirk, W. J. 1970, ApJ, 161, 903
 Miyamoto, M. 1971, PASJ, 23, 21
 Ostriker, J.P., & Peebles, P.J.E. 1973, ApJ, 186, 467
 Pichon, C., & Cannon, R. C. 1997, MNRAS, 291, 616
 Polyachenko, E. V. 2004, MNRAS, 348, 345
 Press, W. H., Teukolsky, S. A., Vetterling, W. T., & Flannery, B. P. 1992, Numerical Recipes (Cambridge: Cambridge Univ. Press)
 Qian, E. E. 1992, MNRAS, 257, 581
 Sawamura, M. 1988, PASJ, 40, 279
 Sellwood, J. A. 1989, MNRAS, 238, 115
 Sellwood, J. A., & Athanassoula, E. 1986, MNRAS, 221, 195
 Stoer, J., & Bulirsch R. 1993, Introduction to Numerical Analysis (New York: Springer)
 Toomre, A. 1963, ApJ, 138, 385
 Toomre, A. 1964, ApJ, 139, 1217
 Toomre, A. 1977, ARA&A, 15, 437
 Toomre, A. 1981, in Structure and Evolution of Normal Galaxies, ed S. M. Fall & D. Lynden-Bell (Cambridge: Cambridge Univ. Press), 111
 Touma, J., & Tremaine, S. 1997, MNRAS, 292, 905
 Tremaine, S., & Weinberg, M. D. 1984, MNRAS, 209, 729
 Vandervoort, P.O. 1999, MNRAS, 303, 393
 Vauterin, P., & Dejonghe, H. 1996, A&A, 313, 465
 Weinberg, M. 1994, ApJ, 421, 481
 Zang, T. A. 1976, PhD Thesis, Massachusetts Institute of Technology, Cambridge, MA
 Zang, T. A., & Hohl, F. 1978, ApJ, 226, 521

APPENDIX

ANGULAR MOMENTUM AND ENERGY

Both the perturbed angular momentum \mathcal{L}_2 and the first component $\mathcal{K}_{2,1}$ of the kinetic energy contain integrals of the form

$$\mathcal{I}_2(t) = \iint S(J_R, J_\phi) f_2 d\mathbf{J}d\Theta, \quad (\text{A1})$$

for different functions S . Such integrals can be evaluated as follows

$$\frac{d\mathcal{I}_2(t)}{dt} = \iint S(J_R, J_\phi) \frac{\partial f_2}{\partial t} d\mathbf{J}d\Theta = \iint S(J_R, J_\phi) \left(\frac{\partial f_2}{\partial t} + [f_2, \mathcal{H}_0] \right) d\mathbf{J}d\Theta, \quad (\text{A2})$$

because the terms added are angle derivatives of periodic functions which integrate to zero over the angles. Equation (6) gives the term in parentheses as the sum of two terms. The first contributes

$$\iint -S[f_0, V_2] d\mathbf{J}d\Theta = \iint S \frac{\partial f_0}{\partial J_\nu} \frac{\partial V_2}{\partial \theta_\nu} d\mathbf{J}d\Theta = \iint \frac{\partial}{\partial \theta_\nu} \left(S V_2 \frac{\partial f_0}{\partial J_\nu} \right) d\mathbf{J}d\Theta = 0. \quad (\text{A3})$$

Here the subscript ν represents the pair of subscripts (R, ϕ) , and we suppose the summation convention to apply to it. The last step again uses the fact that any integral of an integrand which is a derivative with respect to an angle vanishes. The second term contributes

$$\iint -S[f_1, V_1] d\mathbf{J}d\Theta = \iint S \left[\frac{\partial f_1}{\partial J_\nu} \frac{\partial V_1}{\partial \theta_\nu} - \frac{\partial f_1}{\partial \theta_\nu} \frac{\partial V_1}{\partial J_\nu} \right] d\mathbf{J}d\Theta = \iint \left[-f_1 \frac{\partial V_1}{\partial \theta_\nu} \frac{\partial S}{\partial J_\nu} + \frac{\partial V_1}{\partial \theta_\nu} \frac{\partial (S f_1)}{\partial J_\nu} - \frac{\partial (S f_1)}{\partial \theta_\nu} \frac{\partial V_1}{\partial J_\nu} \right] d\mathbf{J}d\Theta. \quad (\text{A4})$$

The combination of the second and third components vanishes because it can be combined to an integral of a divergence:

$$\iint \left[\frac{\partial}{\partial J_\nu} \left(S f_1 \frac{\partial V_1}{\partial \theta_\nu} \right) - \frac{\partial}{\partial \theta_\nu} \left(S f_1 \frac{\partial V_1}{\partial J_\nu} \right) \right] d\mathbf{J}d\Theta. \quad (\text{A5})$$

The second set of component with angle derivatives integrate to zero, but so too do the integrals of derivatives with respect to the actions. That is because the differentiated quantities vanish at the limits in action space, as $J_\phi \rightarrow \pm\infty$ and $J_R \rightarrow \infty$ where the perturbation tends to zero, and at $J_R = 0$ where V_1 is independent of θ_R because $\Psi_{l,j}^m(0, J_\phi) = 0$ for $l \neq 0$ (cf §2.2). The remaining first component of (A4) can be evaluated for $S = J_\phi$ as in (34), to give

$$\frac{d\mathcal{L}_2(t)}{dt} = -2m_s \pi^2 e^{2st} \sum_{l=-\infty}^{\infty} \int d\mathbf{J} \left(l \frac{\partial f_0}{\partial J_R} + m \frac{\partial f_0}{\partial J_\phi} \right) \frac{|\tilde{V}_l|^2}{|l\Omega_R + m\Omega_\phi - \omega|^2}. \quad (\text{A6})$$

This result agrees with that of Lynden-Bell & Kalnajs (1972) when account is taken of the fact that their Fourier coefficients are larger than ours by a factor of $4\pi^2$, and their ω has the opposite sign. For $S = \mathcal{H}_0$, we get

$$\frac{d}{dt} \iint \mathcal{H}_0 f_2 d\mathbf{J}d\Theta = -2s\pi^2 e^{2st} \sum_{l=-\infty}^{\infty} \int d\mathbf{J} \left(l \frac{\partial f_0}{\partial J_R} + m \frac{\partial f_0}{\partial J_\phi} \right) \frac{(l\Omega_R + m\Omega_\phi) |\tilde{V}_l|^2}{|l\Omega_R + m\Omega_\phi - \omega|^2}, \quad (\text{A7})$$

A simple consequence is that

$$\frac{d\mathcal{E}_2}{dt} = \frac{d(\mathcal{K}_2 + \mathcal{W}_2)}{dt} = \Omega_p \frac{d\mathcal{L}_2}{dt}, \quad (\text{A8})$$

where \mathcal{E} is the total energy. The undifferentiated values which are quoted in §2.3 follow because of the simple time dependence on e^{2st} .

A deeper analysis of the second order equation (6), though not its full solution, is needed to evaluate the integral

$$\mathcal{W}_{2,2} = -\mathcal{K}_{2,2} = \iint V_0 f_2 d\mathbf{J}d\Theta. \quad (\text{A9})$$

We rewrite equation (6) as

$$\frac{\partial f_2}{\partial t} + [f_2, \mathcal{H}_0] + [f_0, V_2] = -[f_1, V_1]. \quad (\text{A10})$$

The left hand side of (A10), which is homogeneous in subscript 2 quantities, has the same form as the first order problem for which we derived the homogeneous linear equations (22). Equation (A10) leads in a similar way to inhomogeneous linear equations. Its right hand side contains both axisymmetric terms and non-axisymmetric ones with wavenumber $2m$. We need consider only the axisymmetric terms and the part of the solution for f_2 which they cause, because only they will contribute to the integral (A9) for $\mathcal{W}_{2,2}$. They have a Fourier expansion

$$e^{2st} \sum_{l=-\infty}^{\infty} \tilde{N}_l(J_R, J_\phi) e^{il\theta_R}, \quad \text{where } e^{2st} \tilde{N}_l = \frac{1}{(2\pi)^2} \int d\Theta e^{-il\theta_R} \left(-\frac{1}{4}[f_1, \bar{V}_1] - \frac{1}{4}[\bar{f}_1, V_1] \right). \quad (\text{A11})$$

We represent the potential and density of the axisymmetric part of f_2 by series

$$V_2 = e^{2st} \sum_{j=0}^{\infty} a_j \psi_j^0(R), \quad \Sigma_2 = e^{2st} \sum_{j=0}^{\infty} a_j \sigma_j^0(R), \quad (\text{A12})$$

like those of equations (15) and (16) but now in a complete set of axisymmetric basis functions. We use Fourier expansions

$$f_2 = e^{2st} \sum_{l=-\infty}^{\infty} \tilde{g}_l(J_R, J_\phi) e^{il\theta_R}, \quad V_2 = e^{2st} \sum_{l=-\infty}^{\infty} \tilde{U}_l(J_R, J_\phi) e^{il\theta_R}, \quad (\text{A13})$$

like those of equations (11) and (12), with

$$\tilde{U}_l = \sum_{j=0}^{\infty} a_j \Psi_{l,j}^0, \quad (\text{A14})$$

and with Fourier coefficients $\Psi_{l,j}^0$ defined as in equation (18) for $m = 0$. Matching Fourier coefficients in equation (A10) gives

$$(2s + il\Omega_R) \tilde{g}_l - il \frac{\partial f_0}{\partial J_R} \tilde{U}_l = \tilde{N}_l. \quad (\text{A15})$$

Then, following the same procedure as used in §2.1, we obtain the matrix equation

$$[\mathbf{M}(0, 2is) - \mathbf{D}(0)] \mathbf{a} = \mathbf{h}, \quad (\text{A16})$$

where the components of the column vector \mathbf{h} are given by

$$h_j = 4\pi^2 \sum_{l=-\infty}^{\infty} \int d\mathbf{J} \frac{i\tilde{N}_l \Psi_{l,j}^0}{(l\Omega_R - 2is)}. \quad (\text{A17})$$

The matrix $\mathbf{M}(0, 2is)$ is real because each $\pm l$ pair in the sum (21) combines two complex conjugate quantities, because $\Psi_{l,j}^0$ is even in l [cf eq. (18)]. The right hand side \mathbf{h} of equation (A16) is real because the $\pm l$ pairs in the sum (A17) also combine two complex conjugate quantities, due also to the fact that $\tilde{N}_l = \tilde{N}_{-l}$ because the \tilde{N}_l are the Fourier coefficients of a real function. Hence equation (A16) is a real matrix equation, and its solution for the unknown vector \mathbf{a} is real. Knowing \mathbf{a} , we can evaluate

$$\mathcal{W}_{2,2} = \int V_0 \Sigma_2 d\mathbf{x} = 2\pi e^{2st} \sum_{j=0}^{\infty} a_j \int_0^{\infty} V_0(R) \sigma_j^0(R) R dR. \quad (\text{A18})$$

The reason why it is so much easier to compute $\mathcal{W}_{2,1}$, $\mathcal{K}_{2,1}$, and \mathcal{L}_2 is that they need only the single Fourier coefficient \tilde{g}_0 . Equation (A15) gives \tilde{g}_0 simply as $\tilde{N}_0/2s$ and the matrix equation is not needed.

The computation of \mathbf{a} can be checked by verifying that the total mass due to the axisymmetric density Σ_2 vanishes. This is

$$\mathcal{M}_2(t) = 2\pi e^{2st} \sum_{j=0}^{\infty} a_j \int_0^{\infty} \sigma_j^0(R) R dR = 0. \quad (\text{A19})$$

Formally, the constancy of \mathcal{M}_2 follows from the analysis of Appendix A; it is the $S = 1$ case of integral (A1). With the Clutton-Brock functions (66), the sum (A19) can be evaluated as $(4be^{2st}/G) \sum_{j=0}^{\infty} a_j$ using GR formula (7.225.3).

Substituting the Fourier series (11) and (12) for f_1 and V_1 and carrying out the angle integrations gives

$$i\tilde{N}_l = \frac{1}{4} \sum_{k=-\infty}^{\infty} \left[\left(k \frac{\partial}{\partial J_R} + m \frac{\partial}{\partial J_\phi} \right) \left(\tilde{f}_k \tilde{V}_{k-l} - \tilde{f}_k \tilde{V}_{k+l} \right) - l \left(\tilde{V}_{k-l} \frac{\partial \tilde{f}_k}{\partial J_R} + \tilde{V}_{k+l} \frac{\partial \tilde{f}_k}{\partial J_R} \right) \right] \quad (\text{A20})$$

Derivatives of \tilde{f}_k , and hence second order derivatives of f_0 , are avoided by integrating equation (A17) by parts with respect to the actions. This gives the following integral over the whole action space:

$$h_j = \pi^2 \sum_{l=-\infty}^{\infty} \sum_{k=-\infty}^{\infty} \int d\mathbf{J} \left[- \left(\tilde{f}_k \tilde{V}_{k-l} - \tilde{f}_k \tilde{V}_{k+l} \right) \left(k \frac{\partial}{\partial J_R} + m \frac{\partial}{\partial J_\phi} \right) \left(\frac{\Psi_{l,j}^0}{l\Omega_R - 2is} \right) + l \tilde{f}_k \frac{\partial}{\partial J_R} \left(\frac{\tilde{V}_{k-l} \Psi_{l,j}^0}{l\Omega_R - 2is} \right) + l \tilde{f}_k \frac{\partial}{\partial J_R} \left(\frac{\tilde{V}_{k+l} \Psi_{l,j}^0}{l\Omega_R - 2is} \right) \right]. \quad (\text{A21})$$

For the unidirectional disk with DF (23), h_j is given by the integral (A21) over $J_R \geq 0$, $J_\phi \geq 0$ with $f_0 = f_0^P$, plus the following boundary integral:

$$h_j^B = \pi^2 \sum_{l=-\infty}^{\infty} \sum_{k=-\infty}^{\infty} \int_0^{\infty} dJ_R m f_0^P(J_R, 0) \left[-(\tilde{U}_k \tilde{V}_{k-l} - \tilde{U}_k \tilde{V}_{k+l}) \left(k \frac{\partial}{\partial J_R} + m \frac{\partial}{\partial J_\phi} \right) \left(\frac{\Psi_{l,j}^0}{l\Omega_R - 2is} \right) + l\tilde{U}_k \frac{\partial}{\partial J_R} \left(\frac{\tilde{V}_{k-l} \Psi_{l,j}^0}{l\Omega_R - 2is} \right) + l\tilde{U}_k \frac{\partial}{\partial J_R} \left(\frac{\tilde{V}_{k+l} \Psi_{l,j}^0}{l\Omega_R - 2is} \right) \right]_{J_\phi=0}, \quad (\text{A22})$$

where

$$\tilde{U}_k = \frac{\tilde{V}_k}{k\Omega_R + m\Omega_\phi - \omega}, \quad \tilde{U}_k = \frac{\tilde{V}_k}{k\Omega_R + m\Omega_\phi - \bar{\omega}}. \quad (\text{A23})$$

Note that the solution for $\mathcal{W}_{2,2} = -\mathcal{K}_{2,2}$ intermingle different Fourier components, unlike \mathcal{L}_2 , $\mathcal{W}_{2,1}$, and $\mathcal{K}_{2,1}$ for which the Fourier components can be separated as in equations (35) and (36).

The partial derivatives of $\Psi_{l,j}^m(J_R, J_\phi)$ needed for equations (A21) and (A22) can most easily be calculated simultaneously with the $\Psi_{l,j}^m(J_R, J_\phi)$. For this we differentiate equation (18) partially with respect to an action to obtain

$$\frac{\partial \Psi_{l,j}^m}{\partial J_\nu} = \frac{1}{\pi} \int_0^\pi \left\{ \frac{\partial \psi_j^m}{\partial R} \frac{\partial R}{\partial J_\nu} \cos[l\theta_R + m(\theta_\phi - \phi)] - m\psi_j^m(R) \frac{\partial}{\partial J_\nu} (\theta_\phi - \phi) \sin[l\theta_R + m(\theta_\phi - \phi)] \right\} d\theta_R. \quad (\text{A24})$$

The variables R , $(\theta_\phi - \phi)$, and v_R are to be regarded as functions of (J_R, J_ϕ, θ_R) ; there is no θ_ϕ dependence because of axisymmetry. We use the fact that $v_R = dR/dt = (\partial R/\partial \theta_R)\Omega_R$ to obtain

$$\frac{d}{dt} \left[\frac{\partial R}{\partial J_\nu} \right] = \frac{\partial^2 R}{\partial \theta_R \partial J_\nu} \frac{d\theta_R}{dt} = \Omega_R \frac{\partial}{\partial J_\nu} \left(\frac{\partial R}{\partial \theta_R} \right) = \Omega_R \frac{\partial}{\partial J_\nu} \left(\frac{v_R}{\Omega_R} \right) = \frac{\partial v_R}{\partial J_\nu} - \frac{v_R}{\Omega_R} \frac{\partial \Omega_R}{\partial J_\nu}. \quad (\text{A25})$$

We obtain in a similar way the equations

$$\frac{d}{dt} \left[\frac{\partial}{\partial J_\nu} (\theta_\phi - \phi) \right] = \frac{\partial \Omega_\phi}{\partial J_\nu} - \frac{\delta_{\nu\phi}}{R^2} + \frac{2J_\phi}{R^3} \frac{\partial R}{\partial J_\nu} - \frac{1}{\Omega_R} \left[\Omega_\phi - \frac{J_\phi}{R^2} \right] \frac{\partial \Omega_R}{\partial J_\nu}, \quad (\text{A26})$$

$$\frac{d}{dt} \left[\frac{\partial v_R}{\partial J_\nu} \right] = \frac{2J_\phi}{R^3} \delta_{\nu\phi} - \left[\frac{3J_\phi^2}{R^4} + V_0''(R) \right] \frac{\partial R}{\partial J_\nu} - \frac{1}{\Omega_R} \left[\frac{J_\phi^2}{R^3} - V_0'(R) \right] \frac{\partial \Omega_R}{\partial J_\nu}. \quad (\text{A27})$$

Here $\delta_{\nu\phi}$ is 1 for $\nu = \phi$ and 0 for $\nu = R$. The set of three equations (A25) through (A27) can be added to the others to be integrated for an orbit, and they provide the additional values needed to evaluate the partial derivatives (A24). Initial values are $\partial v_R/\partial J_\nu = \partial(\theta_\phi - \phi)/\partial J_\nu = 0$ at $\theta_R = t = 0$ where $R = R_{\min}$ because $v_R = \theta_\phi - \phi = 0$ there for all orbits. However the initial R_{\min} values change with the actions, and initial values for the derivatives of R with respect to the actions are

$$\left[\frac{\partial R}{\partial J_R} \right]_{R=R_{\min}} = \frac{R_{\min}^3 \Omega_R}{R_{\min}^3 V_0'(R_{\min}) - J_\phi^2}, \quad \left[\frac{\partial R}{\partial J_\phi} \right]_{R=R_{\min}} = \frac{R_{\min} (R_{\min}^2 \Omega_\phi - J_\phi)}{R_{\min}^3 V_0'(R_{\min}) - J_\phi^2}. \quad (\text{A28})$$

They are obtained by differentiating the zeroth order energy equation.

LAGRANGIAN DESCRIPTION, AND BOUNDARY INTEGRALS AS FLUXES

The matrix analysis of §2 uses an Eulerian description of phase space. Kalnajs (1977) gives an alternative Lagrangian description. An advantage of using a Lagrangian description of phase space is that it automatically includes any contributions from the motion of boundaries in phase space. Kalnajs's Lagrangian analysis, with our definition (12) of Fourier coefficients, yields the formula

$$M_{jk}(m, \omega) = -4\pi^2 \sum_{l=-\infty}^{\infty} \int d\mathbf{J} f_0(J_R, J_\phi) \left(l \frac{\partial}{\partial J_R} + m \frac{\partial}{\partial J_\phi} \right) \left[\frac{\Psi_{l,j}^m \Psi_{l,k}^m}{l\Omega_R + m\Omega_\phi - \omega} \right], \quad (\text{B1})$$

with the unperturbed DF f_0 undifferentiated. Our equation (21) follows after integrating (B1) by parts with respect to J_R and J_ϕ . Those integrations introduce boundary terms at any boundary of the region of integration in action space unless one or other of f_0 and the term in square brackets vanish at that boundary. In the case of the wholly prograde DF of equation (23), integration by parts with respect to J_ϕ gives precisely the boundary integral \mathbf{M}^B as defined in (27), plus the area integral (26) after also integrating with respect to J_R . This shows that the boundary integrals, which arise from the step function in the Eulerian description of §2.2, can be explained as due to the motion of that boundary. The boundary integral \mathbf{M}^B arises from the perturbation of a non-zero population of radial orbits.

Lynden-Bell & Kalnajs (1972) had earlier used a Lagrangian analysis to calculate the perturbed angular momentum \mathcal{L}_2 and derived the result

$$\frac{d\mathcal{L}_2(t)}{dt} = 2ms\pi^2 e^{2st} \sum_{l=-\infty}^{\infty} \int d\mathbf{J} f_0(J_R, J_\phi) \left(l \frac{\partial}{\partial J_R} + m \frac{\partial}{\partial J_\phi} \right) \left[\frac{|\tilde{V}_l|^2}{|l\Omega_R + m\Omega_\phi - \omega|^2} \right]. \quad (\text{B2})$$

They then integrated by parts to get an expression for the contribution $L(h_1, h_2)$ to \mathcal{L}_2 from stars with angular momenta in the range (h_1, h_2) . Their result is

$$\begin{aligned} \frac{dL(h_1, h_2)}{dt} = & -2ms\pi^2 e^{2st} \sum_{l=-\infty}^{\infty} \int_{h_1}^{h_2} dJ_\phi \int_0^\infty dJ_R \left(l \frac{\partial f_0}{\partial J_R} + m \frac{\partial f_0}{\partial J_\phi} \right) \left[\frac{|\tilde{V}_l|^2}{|l\Omega_R + m\Omega_\phi - \omega|^2} \right] \\ & + 2m^2 s \pi^2 e^{2st} \sum_{l=-\infty}^{\infty} \int_0^\infty dJ_R \left[\frac{f_0(J_R, J_\phi) |\tilde{V}_l|^2}{|l\Omega_R + m\Omega_\phi - \omega|^2} \right]_{J_\phi=h_1}^{J_\phi=h_2}. \end{aligned} \quad (\text{B3})$$

This formula of an area integral and two boundary integrals is the same as one obtains from applying the Eulerian equation (A6) to the DF $f_0(J_R, J_\phi)H(J_\phi - h_1)H(h_2 - J_\phi)$ which represents the stars with angular momenta in the range (h_1, h_2) . Lynden-Bell & Kalnajs interpret the boundary integrals as representing fluxes through the two boundaries. That interpretation, together with equations (40) and (41) which give a physical significance to the real and imaginary parts of the matrix \mathbf{M} , shows that neglecting the boundary integral terms (27) for a prograde disk of stars means neglecting the contributions to the total potential energy and angular momentum which arise from the perturbation of radial orbits. The numerical results reported in §5.1 shows that this neglect can cause large errors.